

A Spatiotemporal, Quasi-experimental Causal Inference Approach to Characterize the Effects of Global Plastic Waste Export and Burning on Air Quality Using Remotely Sensed Data

Ellen M. Considine^{1*} and Rachel C. Nethery¹

¹Department of Biostatistics, Harvard T.H. Chan School of Public Health

*Email: ellen_considine@g.harvard.edu

Abstract

Open burning of plastic waste may pose a significant threat to global health by degrading air quality, but quantitative research on this problem – crucial for policy making – has been stunted by lack of data. Critically, many low- and middle-income countries, where open burning is of greatest concern, have little to no air quality monitoring. Here, we propose an approach to leverage remotely sensed data products combined with spatiotemporal causal analytic techniques to evaluate the impact of large-scale plastic waste policies on air quality. Throughout, we use the case study of Indonesia before and after 2018, when China halted its import of plastic waste, resulting in diversion of this massive waste stream to other countries. We tailor cutting-edge statistical methods to this setting, estimating effects of the increase in plastic waste imports on fine particulate matter (PM_{2.5}) near waste dump sites in Indonesia as a function of proximity to ports, which serves as an induced continuous exposure. We observe that dump sites above the 20th quantile of port proximity experienced a statistically significant increase in monthly PM_{2.5} concentrations after China’s ban took effect (2018-2019) compared to concentrations expected under business-as-usual (2012-2017), with increases ranging from 0.76–1.72 $\mu\text{g}/\text{m}^3$.

1 Introduction

The open burning of waste, including plastic waste, is an urgent global health issue (Pathak et al., 2024). Open burning is defined as burning “in open fires without managing for the emission of byproducts, such as gases and ash, into the ambient air or soil” (Pathak et al., 2023). An estimated 40-65% of total municipal solid waste is open-burned in low- and middle-income countries (LMICs), largely as a result of two billion people around the world receiving no municipal solid waste collection (Pathak et al., 2024). As will be highlighted in this paper, LMICs also receive large amounts of waste from high-income countries. Regardless of the source of the waste, waste burning threatens public health due to the air pollutants emitted, such as fine particulate matter (Wiedinmyer et al., 2014; Bardales Cruz et al., 2023), abbreviated PM_{2.5}. There is a large body of scientific evidence linking air pollution, and specifically PM_{2.5}, to health consequences ranging from respiratory and cardiovascular disease, to cancer, to reproductive and neurological disorders, to mortality (National Institute of Environmental Health Sciences).

A decade ago, Wiedinmyer et al. (2014) presented the first comprehensive, global estimates of air pollution (and greenhouse gas) emissions due to open waste burning, using an emissions factor approach based on guidelines from the IPCC (Intergovernmental Panel on Climate Change). This approach relies on rough country-level approximations for the amount of waste generated and open-burned, which were derived as a deterministic function of national waste generation rate and waste collection efficiency estimates. The estimated amount of open waste burned was then converted into waste burning-attributable emissions estimates through multiplying by a literature-informed emissions factor. This and other inventories have subsequently been paired with chemical transport modeling to estimate the impact of open burning on regional air quality and attributable mortality (Gordon et al., 2023). While these studies provide evidence that the air pollution contributions of waste burning may be substantial, their methods require strong assumptions backed up by very limited empirical data, and adaptation of these methods to conduct policy impact evaluations, which are crucial for future policy making, would necessitate further strong assumptions about the impact of a policy on the various inputs.

In this study, we focus on plastic waste, whose global generation more than doubled from 2000-2019 (OECD, 2022) and whose transport / trade from higher- to lower-income countries is a major environmental justice issue. In contrast to earlier studies estimating emissions from burning all kinds of waste, recent studies

have focused on more robust estimation of plastic waste generation in specific regions (Bardales Cruz et al., 2023) and detecting molecular tracers from plastic burning (Islam et al., 2022). However, these methods do not easily scale to large regions and/or time periods.

To generate robust empirical evidence about the impacts of plastic waste burning on air quality at scale, here we leverage a case study featuring a large plastic waste quasi-experiment. On January 1, 2018, China banned the import of plastic waste¹. Previously, between 1988 and 2016, they received 45% of global plastic waste exports (Brooks et al., 2018). The 38 OECD (Organisation for Economic Co-operation and Development) countries, most of which are classified as high-income, contributed 64% to all exports in this time frame, with the United States, Japan, and Germany topping the list (Brooks et al., 2018). Unsurprisingly, in the wake of China’s ban there was a marked increase in plastic waste exports to other countries in the East Asia & Pacific region, which were already receiving 30% of global exports (Brooks et al., 2018). In this paper, we focus on Indonesia, which in 2018 became a net importer of plastic waste (Global Plastic Action Partnership, 2020). As of 2020, it was estimated that 48% of Indonesia’s plastic waste is openly burned (Global Plastic Action Partnership, 2020).

In this paper, we seek to quantify the increase in air pollution at open dump sites in Indonesia during 2018–2019 due to (the burning of) increased plastic waste in the wake of China’s 2018 ban. However, data scarcity presents significant obstacles to such an analysis. Indonesia, like many LMICs, has very limited ground-level (“in situ”) air quality monitoring. The country’s first reliable air quality monitors were deployed in Jakarta during our study period (Yosephine, 2016). For context: as of 2020, 51% of the world’s governments did not produce air pollution data (OpenAQ Team, 2020)². In recent years, remotely sensed data have been widely used to fill gaps in in-situ monitoring (Shin et al., 2020). In addition to the lack of air quality data, to our knowledge there is no detailed record of Indonesia’s plastic waste imports along the lines of what Unfried and Wang (2022) used to investigate domestic air quality impacts of China’s ban – and in any case, use of an official record might obscure the contribution of informal and/or covert transportation of waste, which is suggested by analysis of the Indonesian waste sector (Wang and Karasik, 2022). Therefore, we develop an analytic strategy relying on data products derived from remote sensing, including PM_{2.5} estimates, the identification of locations where waste has been openly dumped, and proximity to ports from which plastic waste can enter Indonesia (data sources are detailed in Section 2). To our knowledge, this is the first analysis providing empirical estimates of how a policy-driven change in plastic waste quantity – and associated changes in burning – impacts air quality, in a setting without in-situ air quality monitoring or waste quantity data.

Motivated by this case study, we also propose a new, multiply-robust causal inference approach to estimation and inference for quasi-experimental study designs with a “universal” but dose-dependent intervention. A growing body of work uses quasi-experimental study designs to estimate the air quality impact of a policy or intervention, with a recent surge focused on the Covid-19 lockdown – which resembles our setting in causing a nationwide shift in emissions-relevant behaviors (Heffernan et al., 2024; Chen et al., 2021; Dey et al., 2021). Policies that are adopted “universally” across a country/region of interest present a challenge for many conventional quasi-experimental analytic methods, which typically assume the existence of a control group. To address this, Heffernan et al. (2024) developed a framework for machine learning-based comparative interrupted time series (CITS), in which U.S. city-specific models were used to estimate the difference in average daily air pollution before and after the lockdown dates, using past years of data as controls. A closely related approach was taken by Chen et al. (2021), who used synthetic controls in place of CITS. However, these methods that model each location’s effect separately do not satisfy our needs, because we are interested in characterizing the relationship between changes in air quality and each location’s “dose” of exposure to the treatment / intervention, which in our case is port proximity as defined in Section 2.3. That is, we wish to estimate a causal exposure-response curve.

Our proposed method merges ideas from this literature on quasi-experiments with a “universal” intervention and ideas from the burgeoning literature on multiply-robust causal exposure-response curve estimation. Specifically, we build closely upon recent work by Hettinger et al. (2025), who introduced a multiply-robust estimator for causal exposure-response curves within the difference-in-differences (DiD) framework. Derived from the efficient influence function or EIF (see Section 3.2), this estimator accounts for confounding both between treated and control units and across levels of exposure to the treatment / intervention, which can be thought of as a dosage. We propose a related EIF-based multiply-robust estimator for causal exposure-response curves in quasi-experimental designs with a universal intervention. We also propose an uncertainty quantification approach that accounts for both spatial and temporal correlation. We apply this method to remotely sensed data for the Indonesia plastic waste case study to estimate the change in air pollution at open dump sites due to increased plastic waste in the wake of China’s 2018 ban, as a function of a dump site’s port proximity.

¹China also implemented a second ban in January 2019, tightening its initial policy. However, Unfried and Wang (2022) found that the impact of this second ban was minimal.

²Note that OpenAQ has reported updates to this statistic in 2022 and 2024.

2 Data and Definitions

We compile a monthly analytic dataset spanning 2012-2019, not including more recent years to avoid confounding by the Covid-19 pandemic. This dataset will be made available on Harvard Dataverse post-acceptance of this paper.

2.1 Spatial Units of Analysis: Waste Dump Sites

Waste dump sites serve as our spatial units of analysis in this study. While plastic makes up only 12% of global municipal solid waste, the total aggregation of waste is a key proxy for aggregations of plastic waste (Kruse et al., 2023). Indonesia does not provide official data on dump site locations in the country; thus, we source these data from remote sensing products. Global Plastic Watch (GPW) is a data platform containing satellite imagery-derived classifications of open dump sites, also known as waste aggregations. Kruse et al. (2023) used machine learning to do this classification, and evaluated their performance in Indonesia. The GPW dataset has been used by high-profile groups such as ClimateTrace to estimate emissions from the waste sector (Raniga et al., 2023).

We use all dump sites in Indonesia detected by GPW prior to 2020 for which $PM_{2.5}$ data were available in the Asia region $PM_{2.5}$ data files from van Donkelaar et al. (2021), described below. This results in 356 sites included in our analyses, out of 357 total detected by GPW in Indonesia. Site footprints are provided monthly starting in 2015, but there are frequent gaps and GPW notes that the average across time is more reliable than any given time point. Averaged across time (through the end of 2019), the median area of open dump sites in Indonesia is $2,317m^2$ ($IQR=[881m^2, 5,982m^2]$), but this distribution is highly right-skewed, with a maximum value of $288,424m^2$ ($0.29km^2$).

2.1.1 Why Non-dump Sites Should Not Be Used as “Control” Locations

To motivate our methodological approach (in which we use past years as controls for future years at the GPW dump sites), briefly consider what trying to identify separate “control” locations would look like.

Let us walk through several of the causal identifying assumptions made in Hettinger et al. (2025), which are standard in DiD-type analyses. **Positivity** requires that controls have a non-zero probability of being treated. In our setting, this might be reasonable if we selected non-dump locations with similar characteristics to dump sites, including their proximity to major roads and population density. The **Stable Unit Treatment Value Assumption (SUTVA)** requires that (i) there is no interference between units and (ii) there are no hidden variations in treatment (Rubin, 1980). In our setting, spillover of air pollution becomes a concern if controls are spatially proximate to dump sites, which would be made more likely if we prioritized non-dump locations with similar landcover characteristics. The second aspect of SUTVA might be violated in our case study if we accidentally selected some “control” locations where waste is dumped and burned, but dumping there went undetected in the satellite imagery. **Conditional Parallel Trends** requires that the pre-post difference in the treated group would be the same (conditional on covariates) as that in the control group, in the absence of treatment. Here, consider that Indonesia’s domestic plastic waste generation is increasing by about 5% per year (Global Plastic Action Partnership, 2020). Since we know that a substantial fraction of this waste is taken to dump sites and burned, we would expect the long-term trend in air quality over dump sites to be different than that over non-dump sites, regardless of waste being imported.

Taken together, these considerations illustrate why attempting to use non-dump sites as controls would likely lead to violations of causal identifying assumptions and biased estimates. Thus, we use only waste dump sites in our analysis and assume that they are universally treated by the China plastic waste ban starting in 2018.

2.2 Outcome: Fine Particulate Matter ($PM_{2.5}$) Concentrations

Our outcome of interest is $PM_{2.5}$ concentrations at dump sites. While in-situ measurements are not available across Indonesia, van Donkelaar et al. (2021) estimated global monthly average $PM_{2.5}$ at $0.01^\circ \times 0.01^\circ$ (approximately 1km) resolution using a combination of remotely sensed aerosol optical depth (AOD), chemical transport modeling, and in-situ measurements from around the world. Briefly, they relate AOD to surface $PM_{2.5}$ concentrations using geophysical relationships observed between in-situ $PM_{2.5}$ measurements and AOD simulated from a chemical transport model. They then apply geographically weighted regression to predict (and later adjust for) the residual bias with the in-situ monitors. At monitor sites in Asia from 2015-2019, they report cross-validated R^2 values ranging from 0.59–0.86. Unsurprisingly, estimates over regions with fewer in-situ monitors have higher uncertainty; however, this data is widely used for exposure assessment and epidemiology studies.

We extract these monthly $PM_{2.5}$ values for 2012-2019 at the GPW sites, for each site taking the value of the grid cell in which the site centroid lies. The average $PM_{2.5}$ concentration at the dump sites in 2012-2017 (prior to the China ban) was $25.7 \mu g/m^3$. The time series of concentrations averaged across sites (Figure 1) shows a strong seasonal pattern across our study period.

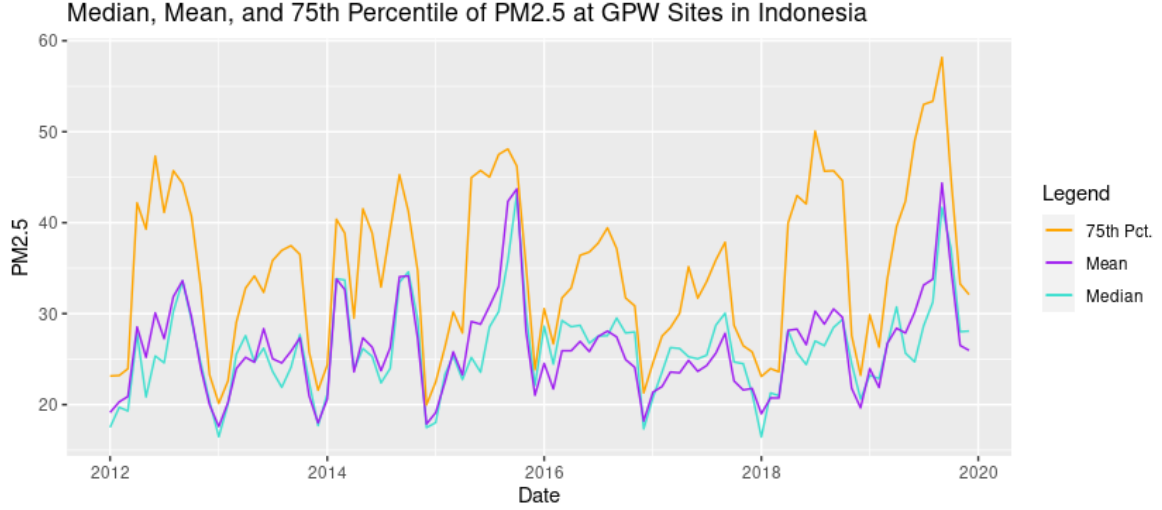


Figure 1: Median, mean, and 75th percentile of $PM_{2.5}$ across GPW sites in Indonesia, 2012-2019.

2.3 Exposure: Port Proximity

Because the policy intervention is on waste imports and in Indonesia any such imports should come through ports, presumably dump sites closer to port activity should be more heavily affected by waste imports. Thus, we consider each dump site's proximity to port activity to be a proxy measure of treatment dose (or "exposure"). Following other recent work assessing the domestic impacts of China's plastic waste ban Unfried and Wang (2022), we could use distance to the nearest port as a proxy. However, that would not take into account the amount of shipping activity in each location. Therefore, we used data from shipping signals remotely sensed via the Automated Identification System, specifically a derived measure of cargo ship loitering from the Global Maritime Traffic Density Service (2021). For our continuous exposure metric, we calculated an inverse-distance-weighted sum of the 2018 loitering data around every GPW site. Due to the strongly right-skewed distribution of this port proximity index, we use a quantile version throughout the analysis, as shown in Figure 2. This transformed variable is henceforth referred to simply as the "port proximity".

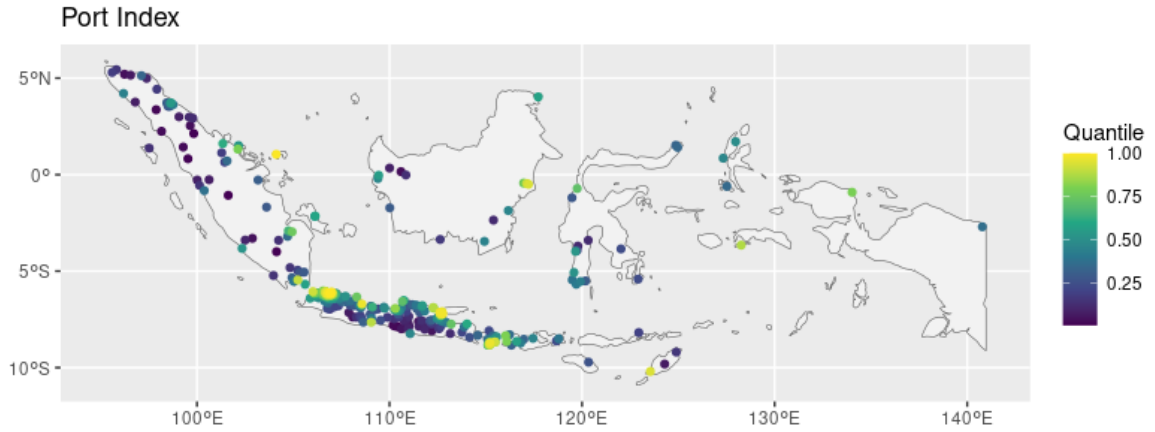


Figure 2: Quantile of the port proximity index for each GPW site in Indonesia.

2.4 Covariates: Meteorology, Population Density, and Fire Locations

As in previous analyses of pre/post-intervention air quality data, the primary covariates in our analyses are meteorological factors (Heffernan et al., 2024; Chen et al., 2021; Dey et al., 2021). By chance, meteorological conditions may differ in the pre- and post-intervention periods, also influencing air quality, and thus failure to adjust for them may bias our estimates of the treatment effects. We obtained ERA5 monthly-aggregated data

for 2012-2019 (Copernicus Climate Change Service, 2017) via Google Earth Engine (Gorelick et al., 2017). This climate reanalysis product, which integrates remotely-sensed and in-situ observations with physics-based models, is available at a spatial resolution of $0.25^\circ \times 0.25^\circ$ (approximately 28km). We take the value at each dump site to be that of the ERA5 grid cell the dump site centroid lies within. We use average air temperature at 2m height, dewpoint temperature at 2m height (indicating humidity), total precipitation, surface pressure, and the u- and v-components of wind speed as covariates in our model.

Population density is another potential confounder in our case study. The GPW API provides an estimate of the population living within 1, 5, and 10 kilometers of each dump site, sourced from WorldPop (Tatem, 2017). Because we observed similar patterns across the sites between these variables, we chose to adjust for population living within 1km for simplicity (it is straightforward to think of this as population density).

Lastly, we obtained the locations of active fires from VIIRS, the Visible Infrared Imaging Radiometer Suite (NASA FIRMS, 2020). The availability of this remotely sensed product (375m resolution daily) starting in 2012 influenced our selection of the study period start. A time series of the total number of active fires across Indonesia is shown in Figure S1. After obtaining the maximum footprint of each dump site as detected by GPW, we performed a spatial overlay of the active fire points. To account for imprecise detection of site boundaries as well as shape fluctuation over time, we used a 100m buffer around each site for the overlay. Throughout our analysis, we consider non-waste dump fires to be those that occurred more than 100m away from any GPW site. We use the monthly count of fires occurring outside of open dump sites in the province as a covariate in our main analysis. The purpose of this is to adjust for potential changes over time in wildfire activity and agricultural burning practices, which could also contribute to changes in $PM_{2.5}$ during the study period.

To assess plausibility that changes in waste burning are contributing to any changes in air quality post-intervention, we conduct a post-hoc exploratory analysis of the temporal trend in the number of VIIRS active fire points at open dump sites in Indonesia during the study period. Increases in active fire points at open dump sites from 2018 onwards would provide informal evidence that changes in air quality may be (at least partially) due to increases in waste burning.

The VIIRS fire overlay also justifies our analysis of all dump site locations from 2012-2019, regardless of when GPW first detected them (prior to 2020). As shown in Figure S2, there were many locations at which major fires occurred prior to their date of first detection as a dump site by GPW. Having observed fires at a site before it was classified as a dump site by GPW increases the likelihood that the site was being used as a dump site prior to the GPW designation.

3 Methods

Analytic code and detailed information on data processing will be made available on GitHub post-acceptance of this paper.

3.1 Setup and Assumptions

Let \mathcal{O} be the observed data, containing: Y the outcome ($PM_{2.5}$), D the dose of exposure (port proximity), and \mathbf{X} the covariates. The latter includes the population living within 1km of the site, monthly averaged meteorology (temperature, humidity, precipitation, pressure, and wind speed), and the number of active fires detected in the province (that month) which did not overlap with any GPW site. To help capture spatial heterogeneity, we also include fixed effects for site ID and province in our model; the spatial boundaries for the latter are shown in Figure S3. Lastly, to account for longer-term trends, we include time $t = 1, \dots, 96$ to represent the months between 2012 and 2019, inclusive.

Furthermore, let B (for “ban”) be a pre- vs. post-intervention indicator. $B = 0$ indicates dates before policy implementation, and $B = 1$ indicates dates after (in our case, 1/1/2018 onwards). Because all units (dump sites) in the analysis are treated post-intervention, B is also a binary indicator of treatment status. We use B rather than the more commonly used A to illustrate this departure from DiD.

Each observation is indexed by its location i ($N = 356$ dump sites) and time point t . When $B_{it} = 0$, we say $D_{it} = \emptyset$, meaning D is undefined – while each location i has a port proximity prior to China’s ban, this feature has not yet been activated to represent the dose of treatment. We define the potential outcomes as $Y_{it}(B_{it} = b, D_{it} = \delta)$, i.e., the outcome that would have been observed for a given unit under intervention status b and dose δ . This definition of the potential outcomes requires that the future cannot affect the past (arrow of time, call this A1) and SUTVA (A2), discussed in section 2.1.1. Mathematically, SUTVA requires that $Y_{it}(\mathbf{B}_t, \mathbf{D}_t) = Y_{it}(B_{it}, D_{it})$, where \mathbf{B}_t and \mathbf{D}_t denote the population-level vectors of intervention and dosage.

Our aim is to estimate a causal exposure-response curve quantifying the causal effect on Indonesian air quality of China’s 2018 plastic waste import ban at different levels of port proximity, δ . In the DiD setting, Hettinger et al. (2025) terms this the “Average Dose Effect on the Treated”, or ADT. While noting again

that our formulation is different, we still see fit to call our effect of interest the ADT:

$$ADT(\delta) = \Psi(\delta) = E[Y(1, \delta) - Y(0, \emptyset) | B = 1]$$

In our case study, this estimand describes the average difference in air quality post-China ban at open dump sites in Indonesia, if all dump sites were exposed to port proximity dose δ . To identify the $ADT(\delta)$, we require

$$(A3) \text{ Consistency: } Y_{it}(b, \delta) = Y_{it} \text{ when } (B_{it}, D_{it}) = (b, \delta)$$

(A4) Positivity: there exists $\epsilon > 0$ such that

$$\begin{aligned} (i) \quad & \epsilon \leq \pi_B(\mathbf{x}) < 1 \quad \forall \mathbf{x} \in \mathbb{X}, \quad \pi_B(\mathbf{x}) = P(B = 1 | \mathbf{x}) \\ (ii) \quad & \epsilon \leq \pi_D(\delta | \mathbf{x}, B = 1) \quad \forall \mathbf{x} \in \mathbb{X} | B = 1, \delta \in \mathbb{D}, \quad \pi_D(\delta | \mathbf{x}, B = 1) = p(D = \delta | B = 1, \mathbf{X} = \mathbf{x}) \end{aligned}$$

In contrast to Hettinger’s Conditional Counterfactual Parallel Trends Between Treated and Control, we require

$$(A5) \text{ Conditional Ignorability Between Time Periods: } E[Y(0, \emptyset) | B = 1, \mathbf{X}] = E[Y(0, \emptyset) | B = 0, \mathbf{X}]$$

This means that there is *no residual time-varying confounding*. Assembling an adequate set of covariates to justify this assumption relies on domain knowledge. Its plausibility can be strengthened by adjusting for seasonal and/or long-term trends, e.g., through inclusion of a time variable in the adjustment set. This assumption is needed due to the absence of control locations in our application.

Lastly, in contrast to Hettinger’s Conditional Counterfactual Parallel Trends Among Treated Between Doses, we require

$$(A6) \text{ Conditional Ignorability Among Treated Between Doses:}$$

$$E[Y(1, \delta) | B = 1, D = \delta, \mathbf{X}] = E[Y(1, \delta) | B = 1, \mathbf{X}] \quad \forall \delta \in \mathbb{D}$$

This means that there is *no residual spatial confounding*, in other words we would expect the post-policy air quality to be the same at all dump sites with covariates \mathbf{X} , if they were assigned dose δ (regardless of their observed port proximity). The plausibility of this assumption may be strengthened by adjusting for region-specific fixed effects (in our case, province).

Assuming these six conditions, our $ADT(\delta)$ is identifiable with observed data:

$$\Psi(\delta) = E[Y(1, \delta) - Y(0, \emptyset) | B = 1] \tag{1}$$

$$= E[E[Y(1, \delta) - Y(0, \emptyset) | B = 1, \mathbf{X}] | B = 1] \tag{2}$$

$$= E[E[Y(1, \delta) | B = 1, D = \delta, \mathbf{X}] - E[Y(0, \emptyset) | B = 0, \mathbf{X}] | B = 1] \tag{3}$$

$$= E[E[Y | B = 1, D = \delta, \mathbf{X}] - E[Y | B = 0, \mathbf{X}] | B = 1] \tag{4}$$

Where line (1) is by definition, (2) by iterated expectations, (3) by A6 on the lefthand side and A5 on the righthand side, and (4) by A1-3.

3.2 Motivations for Efficient Influence Function-Based Estimation

A conventional approach to estimate an exposure-response curve in a quasi-experimental setting would be to use a regression model like this one:

$$E[Y_{it}] = \beta_0 + \beta \mathbf{X}_{it} + \tau B_t + f_\phi(D_{it}) B_t$$

where $f_\phi(D)$ is a flexible (nonparametric) function, with parameters ϕ . There are several drawbacks of this approach. To begin, even if we allow a flexible relationship between D and Y , we are not allowing for flexible relationships between \mathbf{X} and Y , nor interactions between the components of \mathbf{X} . Importantly, we are not addressing confounding between the dose D and trends in the outcome – for instance, if the overall (or seasonal) trend in air pollution is affected by population density, which is static in our dataset and which we know to be correlated with D (see Section 4.2). To address this, we could make a much more complicated linear regression (e.g., by using splines and more interaction terms), or use a nonparametric machine learning algorithm to model Y given D, \mathbf{X}, B . However, this outcome model might still be misspecified. This motivates the search for a doubly-robust estimator, which incorporates both a model for the outcome and a model for the propensity score (the probability of receiving treatment), which explicitly addresses confounding, and will

produce results that are consistent (reliable in a probabilistic sense) if at least one of these models is correctly specified³.

We turn to estimators based on the the Efficient Influence Function (EIF). Without going into the technical details (interested readers should see Kennedy (2022) and Schuler and van der Laan (2023)), the EIF for a specific estimand can be used to construct an estimator that is doubly robust and attains the nonparametric efficiency bound (a nonparametric analog of the Cramer-Rao bound), at least asymptotically. In practice, one has to derive the EIF only for a novel estimand, and in many cases this can build closely on past work. Kennedy et al. (2017) provided a doubly-robust estimation method for causal exposure-response curves in observational data settings, which Hettinger et al. (2025) then extended to a DiD framework, including conditions for “multiple robustness” which will be described in the following section. We further extend this multiply-robust estimator to a setting without control locations, which as described in Section 1 is another common type of quasi-experiment. This work contributes to the nascent application of EIF-based estimation techniques in quasi-experimental settings.

3.3 Estimation

The major difference between our estimator and that of Hettinger et al. (2025) is that instead of modeling the pre-post difference in outcomes, we are just modeling the outcome Y because we are using pre-intervention years rather than separate control locations. This does not substantively change the steps of the proofs in Hettinger et al. (2025) to (1) derive the EIF for the ADT⁴ and (2) show that the resulting estimator is multiply robust. At a high level, after obtaining the EIF, we construct the estimator via the method of estimating equations, which involves setting the EIF equal to zero and solving for Ψ (Schuler and van der Laan, 2023). Given our goal of estimating $\Psi(\delta)$, the relevant parts of this estimator are:

$$\begin{aligned}\xi(D, \mathbf{X}, B, Y; \mu_1, \pi_D) &= B * \left[\frac{f(D|B=1)}{\pi_D(D|\mathbf{X}, B=1)} (Y - \mu_1(D, \mathbf{X})) + m(D|B=1) \right] \\ \tau(\mathbf{X}, B, Y; \mu_0, \pi_B) &= \frac{1}{P(B=1)} \left[\frac{(1-B) * \pi_B(\mathbf{X})}{(1-\pi_B(\mathbf{X}))} (Y - \mu_0(\mathbf{X})) + B * \mu_0(\mathbf{X}) \right]\end{aligned}$$

where

$$\begin{aligned}\mu_0(\mathbf{X}) &= E[Y|B=0, \mathbf{X}] \\ \mu_1(D, \mathbf{X}) &= E[Y|B=1, D, \mathbf{X}] \\ m(D|B=1) &= \int_{\mathbf{X}} \mu_1(D, \mathbf{x}) dP(\mathbf{x}|B=1) = E[Y|B=1, D] \\ f(D|B=1) &= \int_{\mathbf{X}} \pi_D(D|B=1, \mathbf{x}) dP(\mathbf{x}|B=1)\end{aligned}$$

In words: μ_0 and μ_1 are the outcome regressions in the pre- and post-intervention periods, respectively, and $m(D|B=1)$ is the marginalized outcome regression in the post-intervention (treated) period, averaged across the covariates so that it only depends on the dose of exposure D . π_B is the propensity score for being intervened upon (in our case, being in the treated period), π_D is the generalized propensity score (GPS) for receiving dose D of treatment, given being in the treated period, and $f(D|B=1)$ is the marginalized GPS.

Overall, this estimator is unusual in that it has separate functions ξ and τ to estimate the outcome in the presence and absence of treatment – in our case meaning the years after intervention and before intervention respectively. The form of both functions, including both an outcome model and a propensity score-based weight, foreshadows the multiple robustness conditions of this estimator: we need at least one of *each pair* (μ_1, π_D) and (μ_0, π_B) to be correctly specified for the results to be consistent.

To estimate $\Psi(\delta)$, we follow this procedure:

1. Estimate nuisance functions $\mu_1, \mu_0, \pi_B, \pi_D$
2. Calculate $\hat{\xi}(D, \mathbf{X}, B, Y; \hat{\mu}_1, \hat{\pi}_D)$ and $\hat{\tau}(\mathbf{X}, B, Y; \hat{\mu}_0, \hat{\pi}_B)$ on the empirical data using the estimated nuisance functions
3. Regress (smooth) $\hat{\xi}$ on D to obtain $\hat{\Psi}_D(\delta)$, and take the empirical mean of $\hat{\tau}$ to obtain $\hat{\Psi}_0$
4. $\hat{\Psi}(\delta) = \hat{\Psi}_D(\delta) - \hat{\Psi}_0$

³While some papers have questioned the likelihood of either the [generalized] propensity score or outcome model being correctly specified in observational studies, the most well-established alternative to doubly-robust methods for continuous exposures, which utilizes matching (Wu et al., 2024), has been shown to perform poorly when the sample size is small (Cork et al., 2025). And in our application, we only observe 356 unique values of the exposure, one per dump site.

⁴Technically, they derive the EIF for the integral of $ADT(\delta)$ to satisfy the pathwise differentiability requirement.

The estimation of the nuisance functions can be carried out using any flexible modeling technique, e.g., tree ensembles or SuperLearner. Local linear kernel regression (LLKR) is employed for the smooth regression in step 3. The methods and implementation details used in our case study analysis are described in Section 3.5.

3.4 Uncertainty Quantification

For uncertainty quantification, Hettinger et al. (2025) derive a sandwich variance estimator, but mention various limitations of that approach, including that it relies on a normal approximation, that incorporating uncertainty in nuisance function estimation is challenging, and that extensions would be required to account for correlated data. To avoid these complications, here we use a novel variant of the nonparametric bootstrap to obtain pointwise confidence intervals for the ADT. This approach avoids making asymptotic assumptions in our finite sample setting and is designed to respect the complex spatial and temporal correlation structures in our data. Rather than discrete bootstrapping, where observations are either included in a sample or left out entirely, we use weights drawn from an Exponential distribution to allow for small but nonzero inclusion, which helps to improve the observed support of D in the samples (Hettinger et al., 2025). (Note that these weights are scaled to reflect the observed sample sizes in the pre- and post-intervention time periods.) Sampling one weight per location (dump site) rather than per individual observation accounts for temporal correlation across repeated observations. An important extension we propose, motivated by our case study, is to adapt the weights to account for spatial correlation in addition to temporal.

3.4.1 Spatial Weighted Bootstrap

Because our set of covariates likely does not explain all spatial correlation in the data, we need to account for residual spatial dependence in our uncertainty quantification. For instance, note that there are some clusters of dump sites near Jakarta (shown in Figure S4) which we would be hard-pressed to call independent of one another, even conditional on our covariate set. Therefore, in our weighted bootstrap procedure we would like a site’s weight to be larger (or smaller) if other sites nearby have larger (or smaller) weights. We achieve this through *spatially-correlated sampling of the bootstrap weights*.

To build intuition, imagine the following procedure to generate the weights, given a spatial correlation matrix Σ :

1. Sample from a Multivariate Normal distribution with mean zero and variance-covariance (in this case, correlation) matrix Σ .
2. Apply the inverse probability transform to obtain samples with a different (target) marginal distribution, such as the Exponential.

In practice, we can estimate Σ by modeling the empirical spatial variogram of the residuals (see the next section for more details on this estimation and explanation of which model’s residuals are used). This approach of generating bootstrap weights from an estimated spatial correlation function is substantiated by Kurisu et al. (2023), who show the mathematical validity of what they term the spatially dependent wild bootstrap (SDWB). While the SDWB paper assumes a Gaussian random field, they note that this assumption can be relaxed at the expense of additional technical complexity. The issue, described in depth by Tsoukalas et al. (2020), is that the magnitude of correlation is not preserved during the mapping from Gaussian random variables to those from another distribution using the inverse probability transform. To end up with the desired spatial correlation in our Exponential weights, we must first estimate an “equivalent correlation” Σ^* to feed into the Multivariate Normal sampling procedure. Namely, Σ^* should be specified such that, when the Multivariate Normal samples are inverse probability transformed to generate Exponential weights, the resulting weights have the desired spatial correlation (Σ). The estimation of Σ^* can be achieved using numerical integration, which is facilitated by the `anySim` package in R (Tsoukalas et al., 2020).

The complete proposed spatial weighted bootstrap procedure is detailed below.

1. Estimate the empirical variogram of the model residuals and use it to estimate the desired spatial correlation matrix for the weights, Σ (see next section).
2. Estimate the equivalent correlation matrix Σ^* for the desired marginal distribution of the weights (in our case, Exponential).
3. Sample weights \tilde{w}_i (one per site) from a Multivariate Normal distribution with mean zero and variance-covariance matrix Σ^* .
4. Apply the inverse probability transform to \tilde{w}_i to obtain weights w_i with a marginal Exponential distribution and correlation matrix Σ .
5. Use w_i as weights for each observation from location i in the dataset ($t = 1, \dots, 96$), and carry these weights through nuisance function estimation and regression on D to obtain an estimate of the ADT.
6. Repeat steps 3-5 to generate the bootstrap estimates of the ADT.

Point-wise confidence intervals for $ADT(\delta)$ can be formed by extracting the appropriate percentiles (in our case, 2.5 and 97.5) of the estimates across the bootstrap samples.

3.4.2 Estimating the Residual Spatial Correlation Function

In conventional outcome-model-only settings, residual spatial correlation refers to spatial autocorrelation in the residuals obtained from subtracting the model-predicted outcome values \hat{Y} from the observed values Y . In our setting, the precise definition of residual spatial correlation is less evident due to the multiple stages of modeling that go into our estimation: both outcome and propensity score models are plugged into the EIF-derived equations ξ and τ , then $\hat{\xi}$ is regressed on D .

For convenience, let $\hat{\xi}_{it}$ denote $\hat{\xi}(D_{it}, X_{it}, B_{it}, Y_{it})$. Here, we focus on spatial correlation in the residuals $\hat{\xi}_{it} - \hat{\Psi}_D(D_{it})$ for all observations in the treated period $B = 1$. (Note that the counterfactual outcome $\hat{\Psi}_0$ is constant over space.) Intuitively, we address residual spatial correlation from the final stage of modeling because that is the stage in which our effect of interest is estimated, and it represents the “last opportunity” to explain spatial correlation in the data via modeling. From a more technical perspective, Lee et al. (2017) explain that for doubly-robust methods utilizing LLKR, the model-based uncertainty arising from the second-stage estimation (the LLKR) is greater than that of the first-stage estimation (the nuisance models). Additionally, note that in settings like ours where the exposure of interest is spatially explicit, calculating residuals based on the final effect curve (which has been marginalized over all the other covariates) induces a different spatial structure than if we were to analyze residuals $Y_{it} - \hat{\xi}_{it}$.

After calculating the residuals $\hat{\xi}_{it} - \hat{\Psi}_D(D_{it})$, we estimate the empirical variogram using the robust estimator introduced by Cressie and Hawkins (1980), which is less susceptible to influential outliers than the basic method-of-moments approach. We then fit a covariance function, $Cov(m; L, \sigma^2)$, to the empirical variogram, where m is the distance between each pair of sites, L is a bandwidth or “range” parameter, and σ^2 is the magnitude of the variance. The corresponding correlation function $Corr(m; L)$ is obtained by removing the constant σ^2 .

3.4.3 Simulations to Investigate the Spatial Weighted Bootstrap

A pseudo-simulation study was conducted to evaluate the properties of the proposed Spatial Weighted Bootstrap confidence intervals. In Appendix C, we provide full details on the data generating process, the calculation of performance metrics, and the results of this simulation study. Crucially, these simulations illustrate that our Spatial Weighted Bootstrap improves coverage of the confidence intervals relative to a Non-spatial Weighted Bootstrap, across a variety of scenarios.

3.5 Case Study Data Application

In our case study analysis, we use the Ranger algorithm in the `caret` package in R to estimate the nuisance functions, using separate models for $\mu_1, \mu_0, \pi_B, \pi_D$. Details of these models’ hyperparameter tuning and estimation of π_D (the GPS) and $f(D|B = 1)$ are in Appendix A. However, note that while we referred to a common set of covariates (\mathbf{X}) throughout the previous sections, the set of covariates used in the two propensity score models is actually slightly smaller than that described in Section 3.1. The time (month) variable is not included in the model for π_B , because the set of covariates in a flexible machine learning model must not be able to perfectly predict the intervention (Heffernan et al., 2024) – in our case, time steps before and after 1/1/2018. Similarly, the dump site ID is not included in the model for π_D , because the port proximity value is unique to each site. The time variable is also not included in the model for π_D because our port proximity values are static over time.

To regress $\hat{\xi}$ on D (step 3 in the estimation procedure from Section 3.3), we use the `locpol` package in R to perform LLKR with a Gaussian kernel. This package utilizes leave-one-out cross-validation (LOO CV) to select the bandwidth parameter for the kernel regression. Therefore, naively applying the method to our dataset, which contains repeated observations (over time) at each unique value of D (one per dump site), selects an inappropriately small bandwidth. The resulting confidence intervals indicate high instability, as shown in Figure S5. To address this issue, we instead apply the LOO CV to each time step separately (across the 356 dump sites), and then calculate the average bandwidth across the time steps – recall that for the LLKR stage, we are just considering the post-treatment time period $B = 1$. This average bandwidth value is then used in the LLKR model fit on all time points simultaneously.

For the spatial weighted bootstrap, we compared several standard spatial covariance functions (Exponential, Linear, Spherical, and Matérn), ultimately selecting the Matérn as the one with the best RMSE when fit to the empirical variogram of the residuals from the LLKR stage. Therefore, the entries of Σ for our spatially-correlated weights have the form

$$Corr(m; L, \nu) = \frac{2^{1-\nu}}{\Gamma(\nu)} \left(\frac{m}{L}\right)^\nu K_\nu\left(\frac{m}{L}\right)$$

where Γ is the gamma function, K_ν is the modified Bessel function of the second kind, and ν is an additional smoothness parameter which is optimized alongside L .

The empirical spatial range was $\hat{L} = 26.8\text{km}$, and the optimal smoothness parameter was $\hat{\nu} = 0.35$. To gain intuition for the spatially weighted bootstrap, we also ran an analysis ignoring the possibility of spatial

correlation and another using $L = 10\text{km}$ (with the same smoothness $\nu = 0.35$), to span the closely-clustered and numerous-fire sites near Jakarta (shown in Figure S4). The upper lefthand plot in Figure S7 illustrates the resulting magnitudes of correlation between sites at different distances, when using 10km and 26.8km as the spatial range parameter. Confidence intervals for the ADT (with or without spatial correlation in the weights) are calculated using 100 bootstrap samples.

For illustrative purposes, we compare the results from our multiply-robust EIF-based method to (i) a plain outcome regression, which is the same as that used inside the multiply-robust estimator, and (ii) a flexible but confounder-naïve approach. The latter estimates $E[Y|D = \delta, B = 1] - E[Y|B = 0]$, where the first expectation uses the same flexible regression on D as the main method (LLKR) and the second expectation is a sample mean. We also re-ran the analysis using 2017 and, separately, 2016 & 2017 as the “treated” period, to check for pre-trends / policy anticipation (whether the effect began before 2018). Conducting such tests is standard practice for quasi-experiments.

Lastly, while dump site size is not directly accounted for in our main analyses, we conducted a sensitivity analysis to assess how this factor might influence our results, as we thought it could be an important predictor of air pollution heterogeneity across open dump sites. As mentioned in Section 2, Global Plastic Watch estimates the area (footprint) of each dump site. In reality, the dump sites are continuously fluctuating in size, but the measurements at any given time point are less reliable than their average over time; there are also frequent gaps in the remotely sensed detection time series. Therefore, we took the area at each site to be the average across all measurements.

We did not adjust for GPW site size as a covariate in the main analysis because the area of the dump sites as measured after 1/1/18 is technically a post-treatment variable which can be affected by treatment, referred to as a “descendant” of treatment (note that only 68% of the dump sites have at least one area estimate prior to 2018, so we would have to exclude many sites, potentially biasing our causal effect curve, in order to include only pre-2018 area as a covariate). Descendants of treatment should not be conditioned on in causal inference analyses (Hernán and Robins, 2020). We ran a sensitivity analysis to investigate the impact of including site size (averaged across 2012-2019) as a covariate. For simplicity, this sensitivity analysis uses the same nuisance function hyperparameters and spatial range (for the bootstrap weights) as the main analysis.

4 Results

4.1 Statistical Analysis Results

Figure 3 shows the estimated ADT curve and 95% bootstrap confidence interval (CI) from the main analysis. Positive ADT estimates provide evidence of post-China ban increases in $\text{PM}_{2.5}$ concentrations over GPW sites, compared to those expected under business-as-usual. Thus, our results indicate that at open dump sites in Indonesia, the monthly $\text{PM}_{2.5}$ in 2018-2019 was higher than expected under business-as-usual (except for dump sites nowhere near port activity), with the effect ranging from -0.17 – $1.72 \mu\text{g}/\text{m}^3$ (95% CI = $(0.84, 2.66)$ for the maximum value) depending on the port proximity. As expected, we see smaller effects at locations with lower port proximity – the effect is not statistically significantly different from zero until $\delta = 0.2$ (at which $\Psi(\delta) \geq 0.76$), above which it remains significant. The decrease of the effect curve between medium and high levels of port proximity ($\delta \in [0.7, 1]$) could reflect smaller increases in dumping/burning in densely populated areas very close to ports, where there is likely more government oversight and less open space. Integrating across all values of the estimated effect curve yields an average increase at dump sites of $1.14 \mu\text{g}/\text{m}^3$ attributable to China’s ban on plastic imports, corresponding to a 4.4% increase in overall $\text{PM}_{2.5}$ in 2018-2019 compared to 2012-2017. Note that if we only consider dump sites above the 20th quantile of port proximity (where the effect is statistically significant), the average increase is $1.38 \mu\text{g}/\text{m}^3$, corresponding to a 5.1% increase at those sites.

The results from our proposed multiply-robust method are similar to those produced using an outcome regression alone (Figure 3). But variations in both the curve (point estimate) and the confidence interval indicate that it is still important to guard against misspecification of the outcome model by incorporating propensity scores. By contrast, the confounder-naïve results look very different (Figure S6): the mean effect ranges from -6.4 to $7.2 \mu\text{g}/\text{m}^3$. This divergence from our main result is unsurprising, but demonstrative.

The results of using different values as the range parameter for the bootstrap weights’ spatial correlation are shown in Figure S7. A range of 10km produces confidence intervals 74% the width, on average, of those in the main analysis (with a range of 26.8km). Ignoring spatial dependence entirely in the weighted bootstrap narrows the confidence intervals by more than a factor of two (on average, they are 45% the width of those in the main analysis). This demonstrates that accounting for residual spatial correlation is essential to avoid under-estimation of uncertainty in this application.

As shown in Figure 4, we did not observe a significant increase in $\text{PM}_{2.5}$ when using 2017 as the “treated” period (to check for pre-trends / policy anticipation) – in fact, the mean effect is negative, indicating lower $\text{PM}_{2.5}$ in 2017 compared to preceding years. Using 2016 & 2017 as the “treated” period (Figure S8) yields the same conclusion.

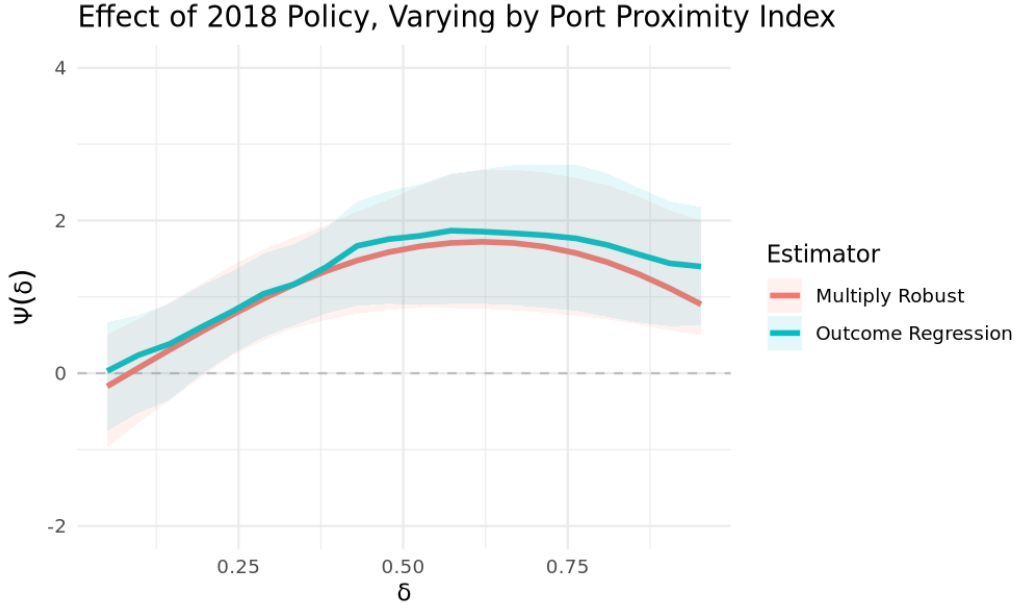


Figure 3: Average dose-effect on the treated (ADT) estimates and bootstrap 95% confidence intervals for our case study, estimated using both our proposed multiply robust method and a conventional outcome regression. ADT estimates (y-axis) quantify the average change in $\text{PM}_{2.5}$ ($\mu\text{g}/\text{m}^3$) post-China ban, compared to concentrations expected under business-as-usual, at open dump sites in Indonesia for a given port proximity (x-axis). The pointwise confidence intervals are generated using our spatial weighted bootstrap with Matérn correlation range=26.8km (as observed in the empirical residuals).

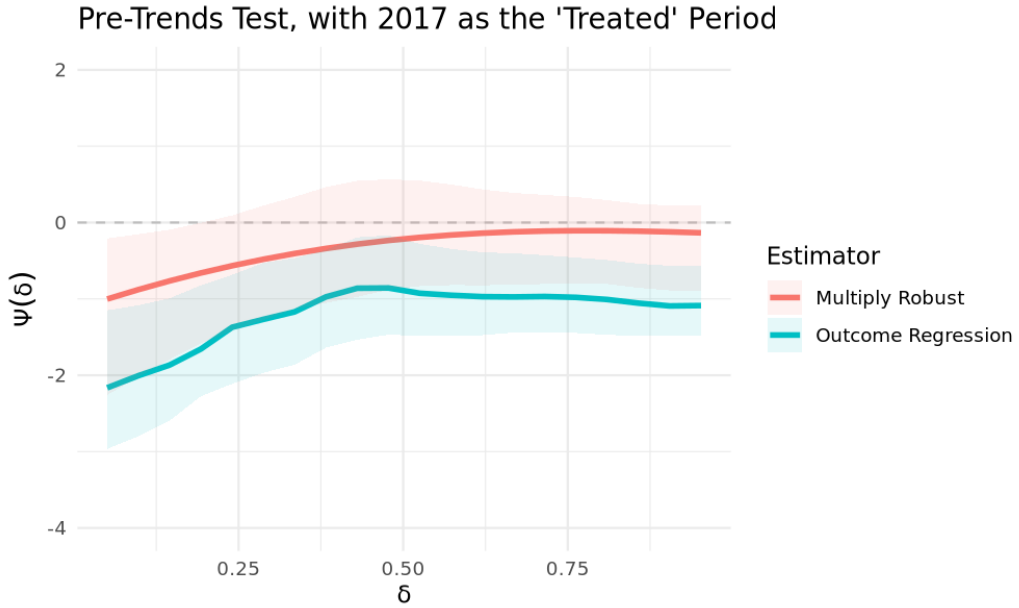


Figure 4: Pre-trends test using 2017 as the “treated” period; sampling bootstrap weights with spatial correlation (range=26.8km).

Including GPW site area as a covariate in our sensitivity analysis did not substantially change the results. The multiply-robust curve in Figure S9 is slightly less peaked (its maximum value is 1.45 rather than 1.72), but the confidence interval widths are practically identical.

4.2 Post-Hoc Exploratory Data Analysis Results

To complement our main analysis, we investigated the occurrence of active fires at the GPW dump sites throughout our study period. Figure 5 shows the time series (aggregated by month) of VIIRS-detected fires overlapping with the dump sites. We observe a large increase in the number of fires in 2018-2019.

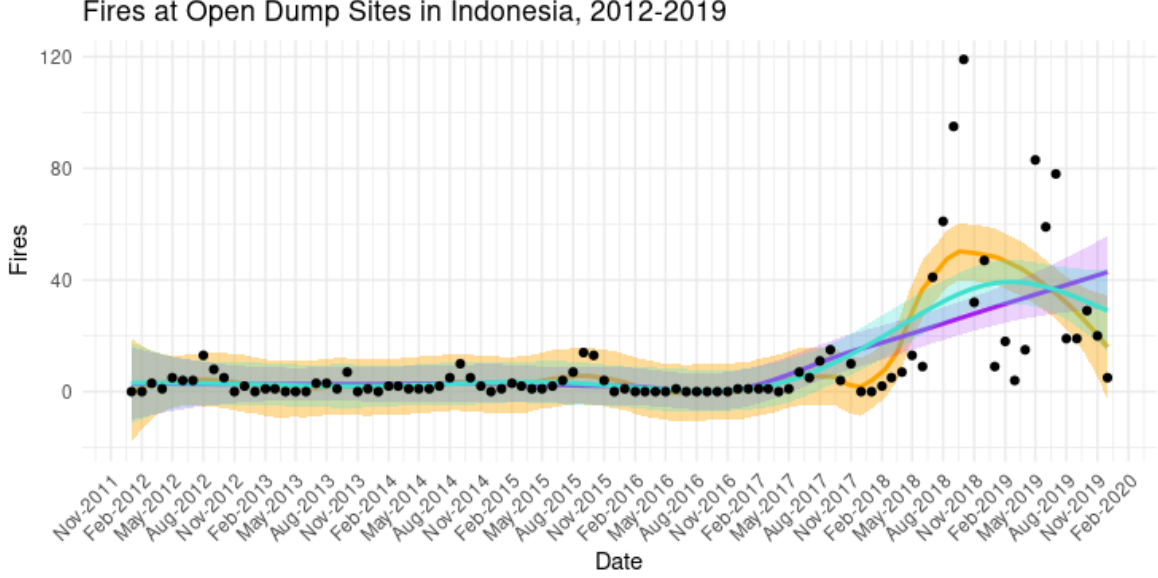


Figure 5: The number of fires detected by VIIRS overlapping with GPW sites (within a 100m buffer) across Indonesia. The colored trend lines are estimated using several different smoothing techniques: the orange using LOESS with span=0.25, the purple using LOESS with span=0.75, and the turquoise using a generalized additive model.

The distribution of the number of fires detected by VIIRS at each dump site is highly skewed, as shown in Figures S3 and S4 (maps of Indonesia overall and the Jakarta region respectively). This is somewhat explained by the area of the dump sites, but not entirely (Figure S10). In keeping with our main analysis, the sites with the most fires are not those with the highest port proximity (Figure S11) – there is a spike around $\delta = 0.7$, due to the cluster of large dump sites to the west of Jakarta, which partially motivated our spatial weighted bootstrap approach. We also note that the correlation between the port proximity and (square root-transformed) population living within 1km of a site is 0.6. While this collinearity might be an issue for estimating our effect of interest in a linear model, it is less of a concern for a doubly-robust nonparametric estimator in which we marginalize over the covariates.

5 Discussion

In this case study, we observed a 4.4% increase in $PM_{2.5}$ at dump sites in Indonesia in 2018-2019 compared to 2012-2017. This effect is on a similar scale to the results of Unfried and Wang (2022), who assessed the domestic impacts of China’s plastic waste import ban and estimated an average reduction of $3.7 \mu g/m^3$, corresponding to 8.5% reduction of overall $PM_{2.5}$ concentrations in China as a result of their 2018 ban. It makes sense that our observed effect would be smaller, given that Indonesia was only one of the countries to which waste that would otherwise have gone to China was diverted. Unfried and Wang (2022) similarly did not observe an anticipation effect in mid-2017, when China announced its upcoming ban to the World Trade Organization.

Methodologically, we demonstrate the viability of pairing spatiotemporal causal inference methods with remotely sensed data products to quantify the air quality impacts of large-scale plastic waste policies via the mechanism of waste burning. On the data side, we harmonize areal classifications of open dump sites, cargo ship loitering densities, meteorologic estimates, active fire points, and high-resolution air pollution estimates. For the statistical analysis, we combine a multiply-robust estimator for causal exposure-response curves within the difference-in-differences framework with the technique of using pre-intervention years as controls for post-intervention years. Additionally, we illustrate the importance of accounting for spatial dependence in the uncertainty quantification stage, and propose a spatial weighted bootstrap approach for doing so. Given that there are numerous documented quasi-experiments created by plastic waste policies globally (Karasik et al., 2023), which have largely occurred in countries lacking in-situ air quality monitoring data, we anticipate that the analytic framework developed here can be much more widely applied.

This study has a few limitations which merit remarks. First, while we are focused on the air quality impact of China’s 2018 ban and resultant increase in plastic waste in Indonesia, the observed difference between 2018-2019 and 2012-2017 might be affected by another policy that was implemented around the same time (2017-2018): Indonesia’s National Action Plan on Marine Plastic Debris. The goal of this policy was to reduce the amount of plastic waste ending up in the ocean – with limited emphasis on reducing the amount of plastic waste being generated (Arifin et al., 2023); by 2021 Indonesia achieved an estimated 15% reduction of marine plastic debris from 2017 levels (Wang and Karasik, 2022). Ethnographic studies from around the world have found that campaigns to raise awareness about plastic pollution often contribute to increased open burning, as communities seek to cut down on litter and deal with waste that has been collected (Pathak et al., 2024). Hence, it is possible that these two policies were interacting to generate the observed increase in $PM_{2.5}$ at dump sites in Indonesia. Our analysis showing no pre-trends effect when using 2017 as the “treated” year guards against this possibility somewhat, however the effect of the National Action Plan could lag or increase after 2017.

Second, while our interest is primarily on air pollution generated by the burning of waste, it is possible that some of the observed increase in $PM_{2.5}$ at open dump sites is attributable to the *transportation* of this waste, for instance from diesel trucks making more trips to dump sites and, for sites close to the coast, from cargo ships. Our post-hoc analysis illustrating the uptick in active fires overlapping with dump sites offers some evidence that at least part of the observed effect could plausibly be due to increases in waste burning. Unfortunately, speciated $PM_{2.5}$ estimates, which might enable the disentangling of emissions from waste burning and transportation, tend to be available only at coarse spatiotemporal resolutions globally and rely more heavily on models (European Commission, Joint Research Centre, 2023), which is likely to frustrate the application of quasi-experimental statistical methods. For smaller scale studies, Islam et al. (2022) demonstrated the viability of measuring a molecular tracer of plastic burning with in-situ monitors. Alternatively, Scott et al. (2023) applied machine learning-based image classification to identify smoke plumes in high-resolution (3m x 3m) satellite imagery over the largest municipal landfill in the Maldives. However, in addition to being computationally intensive, this approach is not directly translatable into air pollution concentrations, which are easier to link to the rich literature on health impacts, and hence tend to be more relevant for policy makers.

Third, while remotely sensed data products enable application of quasi-experimental methods in data-scarce settings, we must be conscious of their potential for measurement error / misclassification. In this case study, we believe that the GPW dump site classifications are the data product in which errors would be most consequential for our analysis. Because all the GPW sites detected in Indonesia were manually validated (Kruse et al., 2023), there should be no false positive classifications. However, false negative classifications are possible and could affect our analysis in two ways. On the one hand, because we include the number of active fires in each province *not overlapping with dump sites* as a covariate in \mathbf{X} , any fires mistakenly classified as non-dump fires will reduce our estimated policy effect. On the other hand, if there is spillover of $PM_{2.5}$ from false negative dump sites to nearby GPW-detected dump sites, then this could increase our estimated *per-site* policy effect.

A more general limitation of our approach is that we cannot estimate the effects of distributed waste burning, i.e., at the household level or at communal dump sites that were too small to be detected by GPW. Future research, and likely investment in ground-level air quality monitors (and/or lower cost sensors), will be needed to estimate these distributed burning emissions, which may ultimately pose greater risks to public health due to higher frequency of burning, greater proximity to people, and lower dispersive dilution of air pollution at the ground level (Pathak et al., 2024) compared to taller plumes of smoke resulting from larger fires at larger dump sites.

Despite its limitations, this study provides strong evidence that the export of plastic waste to Indonesia, and subsequent open burning of import-related waste in Indonesia, has resulted in higher concentrations of $PM_{2.5}$ – at least near large open dump sites. This motivates future policies to (a) reduce the amount of plastic waste being exported from the Global North to the Global South and (b) reduce the amount of waste being openly burned. Both will require substantial investments in waste management infrastructure and/or dramatic shifts in the amount of plastic waste being generated. With respect to waste burning, it has been observed that simply prohibiting open burning is seldom effective (Pathak et al., 2024), though burning at major sites may be easier to monitor and restrict (Scott et al., 2023).

On the global stage, negotiations by the United Nations are currently underway to develop a Global Plastic Treaty – with an international legally binding instrument on plastic pollution (United Nations Environment Programme (UNEP), 2024) – under the Basel Convention on the Control of Transboundary Movements of Hazardous Wastes and Their Disposal. The effectiveness of this and future policies, at least for improving air quality but potentially also for other kinds of environmental outcomes, can in turn be evaluated using methods similar to those presented in this paper.

Acknowledgements

This work was supported by an NSF Graduate Research Fellowship (EMC), NIH award K01ES032458 (RCN), and the Harvard Climate Change Solutions Fund (RCN). The computation for this paper was performed on the FASRC Cannon cluster supported by the FAS Division of Science Research Computing at Harvard University.

We would like to thank the National Studies on Air Pollution and Health research group for their feedback and support. Additionally, we thank Christine Wiedinmyer and Randall Martin for early input on the project direction, and the Nafas team for sharing their knowledge of the air quality monitoring, evaluation, and regulatory landscape in Indonesia.

References

- Arifin, Z., Falahudin, D., Saito, H., Mintarsih, T. H., Hafizt, M., and Suteja, Y. Indonesian policy and researches toward 70 *Marine Policy*, 155:105692, 2023. ISSN 0308-597X. doi: <https://doi.org/10.1016/j.marpol.2023.105692>. URL <https://www.sciencedirect.com/science/article/pii/S0308597X23002191>.
- Bardales Cruz, M., Saikawa, E., Hengstermann, M., Ramirez, A., McCracken, J. P., and Thompson, L. M. Plastic waste generation and emissions from the domestic open burning of plastic waste in Guatemala. *Environmental Science: Atmospheres*, 3(1):156–167, 2023. ISSN 2634-3606. doi: 10.1039/D2EA00082B. URL <https://xlink.rsc.org/?DOI=D2EA00082B>.
- Brooks, A. L., Wang, S., and Jambeck, J. R. The Chinese import ban and its impact on global plastic waste trade. *Science Advances*, 4(6):eaat0131, Jun 2018. doi: 10.1126/sciadv.aat0131.
- Chen, K. L., Henneman, L. R. F., and Nethery, R. C. Differential impacts of COVID-19 lockdowns on PM2.5 across the United States. *Environmental Advances*, 6:100122, Dec. 2021. ISSN 2666-7657. doi: 10.1016/j.envadv.2021.100122. URL <https://www.sciencedirect.com/science/article/pii/S2666765721000934>.
- Copernicus Climate Change Service. ERA5: Fifth generation of ECMWF atmospheric reanalyses of the global climate. Copernicus Climate Change Service (C3S) Climate Data Store (CDS), 2017. URL https://developers.google.com/earth-engine/datasets/catalog/ECMWF_ERA5_MONTHLY. Accessed: 2024-09-06.
- Cork, M., Mork, D., and Dominici, F. Methods for Estimating the Exposure-Response Curve to Inform the New Safety Standards for Fine Particulate Matter. *Journal of the Royal Statistical Society Series A: Statistics in Society*, Jan. 2025. URL <https://academic.oup.com/jrssa/advance-article-abstract/doi/10.1093/jrssa/qnaf004/7958788>.
- Cressie, N. and Hawkins, D. M. Robust estimation of the variogram: I. *Journal of the international Association for Mathematical Geology*, 12:115–125, 1980.
- Dey, T., Tyagi, P., Sabath, M. B., Kamareddine, L., Henneman, L., Braun, D., and Dominici, F. Counter-factual time series analysis of short-term change in air pollution following the covid-19 state of emergency in the united states. *Scientific Reports*, 11(1):23517, 2021.
- van Donkelaar, A., Hammer, M. S., Bindle, L., Brauer, M., Brook, J. R., Garay, M. J., Hsu, N. C., Kalashnikova, O. V., Kahn, R. A., Lee, C., Levy, R. C., Lyapustin, A., Sayer, A. M., and Martin, R. V. Monthly Global Estimates of Fine Particulate Matter and Their Uncertainty. *Environmental Science & Technology*, 55(22):15287–15300, Nov. 2021. ISSN 0013-936X. doi: 10.1021/acs.est.1c05309. URL <https://doi.org/10.1021/acs.est.1c05309>. Publisher: American Chemical Society.
- European Commission, Joint Research Centre. EDGAR - Emissions Database for Global Atmospheric Research: v8.1, 2023. URL https://edgar.jrc.ec.europa.eu/dataset_ap81. Accessed: 2024-10-23.
- Global Maritime Traffic Density Service. GMTDS Data. <https://www.globalmaritimetraffic.org>, 2021. A service of MapLarge. Accessed ship loitering data on 2024-09-05.
- Global Plastic Action Partnership. Radically Reducing Plastic Pollution in Indonesia: A Multistakeholder Action Plan National Plastic Action Partnership. Technical report, World Economic Forum, 2020. URL <https://weforum.ent.box.com/s/3dx0h6h3iyab847msnx7iw62kjt5myu>. Accessed: 2024-10-08.
- Gordon, J. N. D., Bilsback, K. R., Fiddler, M. N., Pokhrel, R. P., Fischer, E. V., Pierce, J. R., and Bililign, S. The Effects of Trash, Residential Biofuel, and Open Biomass Burning Emissions on Local and Transported PM2.5 and Its Attributed Mortality in Africa. *GeoHealth*, 7(2):e2022GH000673, 2023. ISSN 2471-1403. doi: 10.1029/2022GH000673. URL <https://onlinelibrary.wiley.com/doi/abs/10.1029/2022GH000673>. eprint: <https://onlinelibrary.wiley.com/doi/pdf/10.1029/2022GH000673>.
- Gorelick, N., Hancher, M., Dixon, M., Ilyushchenko, S., Thau, D., and Moore, R. Google Earth Engine: Planetary-scale geospatial analysis for everyone. *Remote Sensing of Environment*, 202:18–27, 2017. ISSN 0034-4257. doi: <https://doi.org/10.1016/j.rse.2017.06.031>. URL <https://www.sciencedirect.com/science/article/pii/S0034425717302900>. Big Remotely Sensed Data: tools, applications and experiences.
- Heffernan, C., Koehler, K., Zamora, M. L., Buehler, C., Gentner, D. R., Peng, R. D., and Datta, A. A causal machine-learning framework for studying policy impact on air pollution: A case-study in COVID-19 lockdowns. *American Journal of Epidemiology*, page kwae171, Jul 2024. doi: 10.1093/aje/kwae171. Epub ahead of print.

- Hernán, M. A. and Robins, J. M. *Causal Inference: What If*. Chapman & Hall/CRC, Boca Raton, 2020. URL <https://www.hsph.harvard.edu/miguel-hernan/causal-inference-book/>.
- Hettinger, G., Lee, Y., and Mitra, N. Multiply robust difference-in-differences estimation of causal effect curves for continuous exposures. *Biometrics*, 81(1):ujaf015, 02 2025. ISSN 0006-341X. doi: 10.1093/biometc/ujaf015. URL <https://doi.org/10.1093/biometc/ujaf015>.
- Islam, M. R., Welker, J., Salam, A., and Stone, E. A. Plastic Burning Impacts on Atmospheric Fine Particulate Matter at Urban and Rural Sites in the USA and Bangladesh. *ACS Environmental Au*, 2(5):409–417, Sept. 2022. ISSN 2694-2518, 2694-2518. doi: 10.1021/acsenvironau.1c00054. URL <https://pubs.acs.org/doi/10.1021/acsenvironau.1c00054>.
- Karasik, R., Virdin, J., and Wilson, J. Plastics Policy Inventory. <https://nicholasinstitute.duke.edu/plastics-policy-inventory/>, 2023. Accessed: 2024-10-30.
- Kennedy, E. H. Semiparametric Doubly Robust Targeted Double Machine Learning: A Review. *arXiv preprint arXiv:2203.06469*, 2022. URL <https://arxiv.org/abs/2203.06469>.
- Kennedy, E. H., Ma, Z., McHugh, M. D., and Small, D. S. Nonparametric methods for doubly robust estimation of continuous treatment effects. *Journal of the Royal Statistical Society: Series B (Statistical Methodology)*, 79(4):1229–1245, Sep 2017. doi: 10.1111/rssb.12212.
- Kruse, C., Boyda, E., Chen, S., Karra, K., Bou-Nahra, T., Hammer, D., Mathis, J., Maddalene, T., Jambeck, J., and Laurier, F. Satellite Monitoring of Terrestrial Plastic Waste. *PLOS ONE*, 18(1):e0278997, Jan. 2023. ISSN 1932-6203. doi: 10.1371/journal.pone.0278997. URL <http://arxiv.org/abs/2204.01485>. arXiv:2204.01485 [cs, eess].
- Kurusu, D., Kato, K., and Shao, X. Gaussian Approximation and Spatially Dependent Wild Bootstrap for High-Dimensional Spatial Data. *Journal of the American Statistical Association*, pages 1–13, July 2023. ISSN 0162-1459, 1537-274X. doi: 10.1080/01621459.2023.2218578. URL <https://www.tandfonline.com/doi/full/10.1080/01621459.2023.2218578>.
- Lee, S., Okui, R., and Whang, Y.-J. Doubly robust uniform confidence band for the conditional average treatment effect function. *Journal of Applied Econometrics*, 32(7):1207–1225, 2017. doi: <https://doi-org.ezp-prod1.hul.harvard.edu/10.1002/jae.2574>. URL <https://onlinelibrary-wiley-com.ezp-prod1.hul.harvard.edu/doi/abs/10.1002/jae.2574>.
- NASA FIRMS. Viirs Active Fire (375m S-NPP, 2012-2019). https://firms.modaps.eosdis.nasa.gov/active_fire/, 2020. Accessed: 2024-06-18.
- National Institute of Environmental Health Sciences. Air pollution and your health. URL <https://www.niehs.nih.gov/health/topics/agents/air-pollution>. Accessed: October 22, 2024.
- OECD. Plastic Pollution is Growing Relentlessly as Waste Management and Recycling Fall Short. <https://www.oecd.org/en/about/news/press-releases/2022/02/plastic-pollution-is-growing-relentlessly-as-waste-management-and-recycling-fall-short.html>, 2022. Accessed: 2024-10-30.
- OpenAQ Team. Open Air Quality Data: The Global State of Play. Technical report, OpenAQ, 2020. URL <https://documents.openaq.org/reports/Open+Air+Quality+Data+Global+State+of+Play+2020.pdf>. Accessed: 2025-04-08.
- Pathak, G., Nichter, M., Hardon, A., Moyer, E., Latkar, A., Simbaya, J., Pakasi, D., Taqeban, E., and Love, J. Plastic pollution and the open burning of plastic wastes. *Global Environmental Change*, 80: 102648, 2023. ISSN 0959-3780. doi: <https://doi.org/10.1016/j.gloenvcha.2023.102648>. URL <https://www.sciencedirect.com/science/article/pii/S0959378023000146>.
- Pathak, G., Nichter, M., Hardon, A., and Moyer, E. The Open Burning of Plastic Wastes is an Urgent Global Health Issue. *Annals of Global Health*, 90(1):3, 2024. ISSN 2214-9996. doi: 10.5334/aogh.4232. URL <https://www.ncbi.nlm.nih.gov/pmc/articles/PMC10786097/>.
- Raniga, K., Davitt, A., Lewis, C., Sridhar, L., Gans, L., and McCormick, G. Waste Sector: Estimating CH₄ Emissions from Solid Waste Disposal Sites, 2023. URL <https://github.com/climatetracecoalition/methodology-documents/blob/main/2023/Waste/Waste%20Sector-%20Emissions%20from%20Solid%20Waste%20Disposal%20Site%20methodology.docx.pdf>. Emissions modeling by WattTime.
- Rubin, D. B. Randomization analysis of experimental data: The fisher randomization test comment. *Journal of the American Statistical Association*, 75(371):591–593, 1980.

- Schuler, A. and van der Laan, M. *Introduction to Modern Causal Inference*. 2023. Available at <https://alejandroschuler.github.io/mci>.
- Scott, S. R., Hailemariam, P. E., Bhawe, P. V., Bergin, M. H., and Carlson, D. E. Identifying Waste Burning Plumes Using High-Resolution Satellite Imagery and Machine Learning: A Case Study in the Maldives. *Environmental Science & Technology Letters*, 10(8):642–648, Aug. 2023. doi: 10.1021/acs.estlett.3c00225. URL <https://doi.org/10.1021/acs.estlett.3c00225>. Publisher: American Chemical Society.
- Shin, M., Kang, Y., Park, S., Im, J., Yoo, C., and Quackenbush, L. J. Estimating ground-level particulate matter concentrations using satellite-based data: a review. *GIScience & Remote Sensing*, 57(2):174–189, 2020. doi: 10.1080/15481603.2019.1703288. URL <https://doi.org/10.1080/15481603.2019.1703288>.
- Tatem, A. J. WorldPop, open data for spatial demography. *Scientific Data*, 4(1):170004, Jan. 2017. ISSN 2052-4463. doi: 10.1038/sdata.2017.4. URL <https://doi.org/10.1038/sdata.2017.4>.
- Tsoukalas, I., Kossieris, P., and Makropoulos, C. Simulation of Non-Gaussian Correlated Random Variables, Stochastic Processes and Random Fields: Introducing the anySim R-Package for Environmental Applications and Beyond. *Water*, 12(6), 2020. ISSN 2073-4441. doi: 10.3390/w12061645. URL <https://www.mdpi.com/2073-4441/12/6/1645>.
- Unfried, K. and Wang, F. Importing Air Pollution? Evidence from China’s Plastic Waste Imports. 2022.
- United Nations Environment Programme (UNEP). Addressing Global Plastic Pollution: A Timeline Leading up to the Intergovernmental Negotiating Committee, 2024. URL <https://www.unep.org/inc-plastic-pollution/about/history>. Accessed: 2024-10-23.
- Wang, Y. and Karasik, R. Plastic Pollution Policy Country Profile: Indonesia. Technical Report NI PB 22-05, Duke University, Durham, NC, 2022.
- Wiedinmyer, C., Yokelson, R. J., and Gullett, B. K. Global Emissions of Trace Gases, Particulate Matter, and Hazardous Air Pollutants from Open Burning of Domestic Waste. *Environmental Science & Technology*, 48(16):9523–9530, Aug. 2014. ISSN 0013-936X. doi: 10.1021/es502250z. URL <https://doi.org/10.1021/es502250z>. Publisher: American Chemical Society.
- Wu, X., Mealli, F., Kioumourtoglou, M.-A., Dominici, F., and Braun, D. Matching on generalized propensity scores with continuous exposures. *Journal of the American Statistical Association*, 119(545):757–772, 2024. doi: 10.1080/01621459.2022.2144737. URL <https://doi.org/10.1080/01621459.2022.2144737>. PMID: 38524247.
- Yosephine, L. U.S. embassy, Jakarta cooperate to monitor air quality. *The Jakarta Post*, May 17 2016. URL <https://www.thejakartapost.com/news/2016/05/17/us-embassy-jakarta-cooperate-to-monitor-air-quality.html>.

A Estimation Details

A.1 Nuisance Function Hyperparameters

For each of the nuisance functions $(\mu_1, \mu_0, \pi_B, \pi_D)$, we use the Ranger algorithm (from the R `caret` package) with `num.trees=500`. For the regressions (all but π_B , which is a binary classification), we use `min.node.size=5` and select the minimum value of `mtry` (the number of variables to possibly split at in each node) beyond which the R^2 and RMSE do not substantially improve (a difference within 0.01 for R^2 and 0.1 for RMSE). For π_B , we limit `mtry` such that the empirical probabilities do not get too large (>0.99) or too small (<0.001).

To prevent overfitting, we use cross-validation with $k=2$ folds to select `mtry`. For μ_0 , we sample observations into the folds by year block (2012 & 2013, 2014 & 2015, 2016 & 2017) to emulate this model's extrapolation to the $B = 1$ years. For π_D , we sample observations by GPW site to account for D being a static variable in our dataset, even though \mathbf{X} contains some time-varying covariates. For μ_1 and π_B , we randomly sample observations from $\mathcal{O}_{B=1}$ and \mathcal{O} respectively.

A.2 Generalized Propensity Score (GPS) Estimation

Following the GPS estimation method utilized by Wu et al. (2024), we first fit a model to D given \mathbf{X} , within $B = 1$. Note that while in our dataset, D is static (derived from the 2018 GMTDS data), early experimentation revealed that the time-varying covariates are meaningfully predictive of D . Our intuition for this is that the spatial variation in the *average* values of the meteorological covariates, such as humidity, is informative of how close one is to the coast, which is in turn associated with port proximity.

After fitting the initial model for D , we fit a model to the residuals $D_i - \hat{D}_i$ given \mathbf{X} , within $B = 1$. (For efficiency, we use the same hyperparameters for this residual model as for the initial model of D .) Then, we apply a kernel density estimator to $(D_i - \hat{D}_i)/\hat{\epsilon}_i$ to obtain π_D . For $f(D|B=1) = \int_{\mathbf{x}} \pi_D(D|B=1, \mathbf{x}) dP(\mathbf{x}|B=1)$, we interpolate over the observed \mathbf{X} for specified values of D .

B Supplementary Figures and Tables

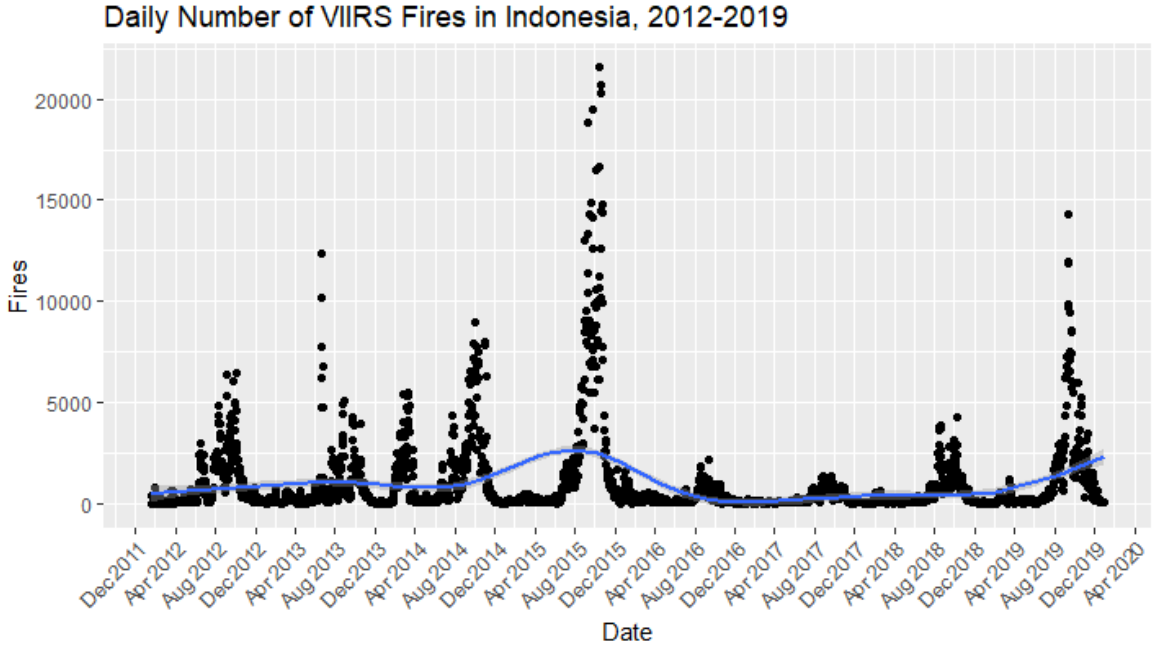


Figure S1: Sum of daily VIIRS fires detected anywhere in Indonesia (not only at waste dump sites), with smoothed trend shown.

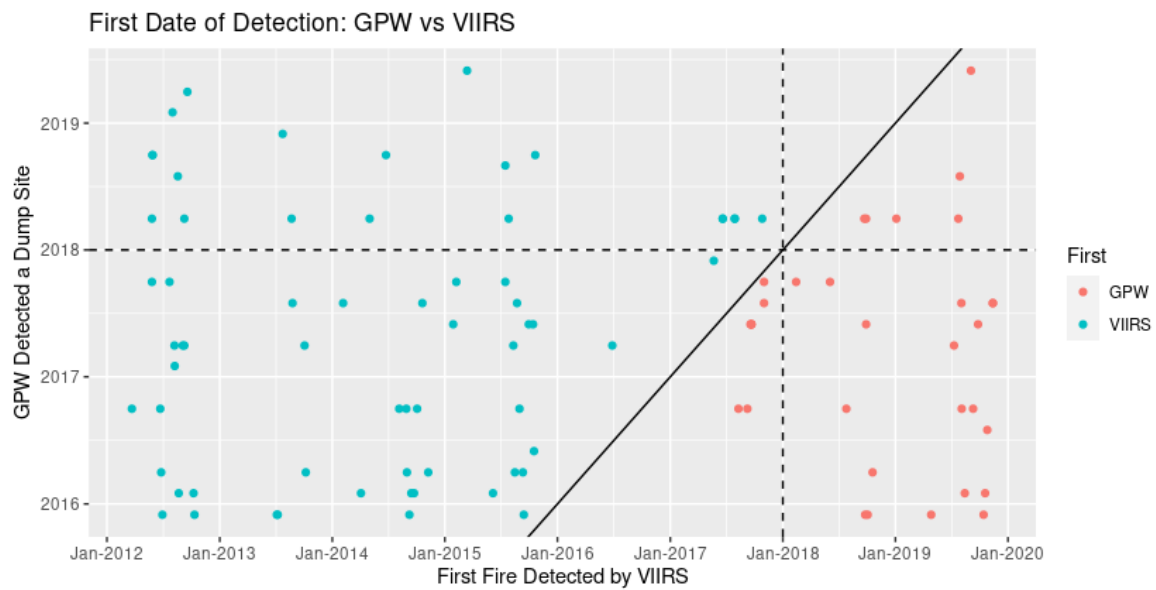


Figure S2: Detection date of each dump site (at which active fires occurred) based on GPW's algorithm and VIIRS.

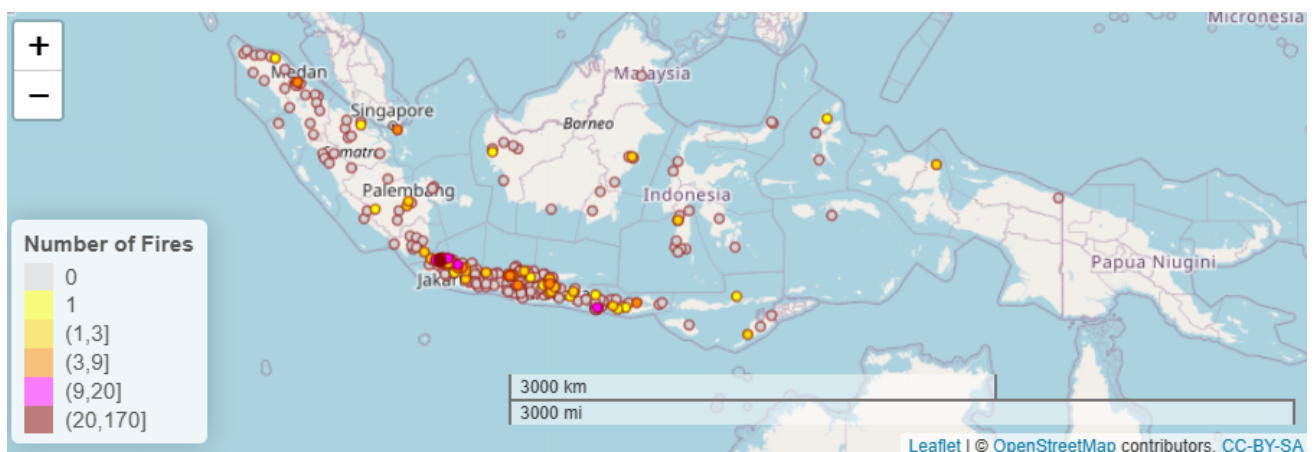


Figure S3: Map of Indonesia showing the number of fires detected by VIIRS overlapping with each dump site (detected by Global Plastic Watch) in 2012-2019 and the boundaries of the provinces (in gray).

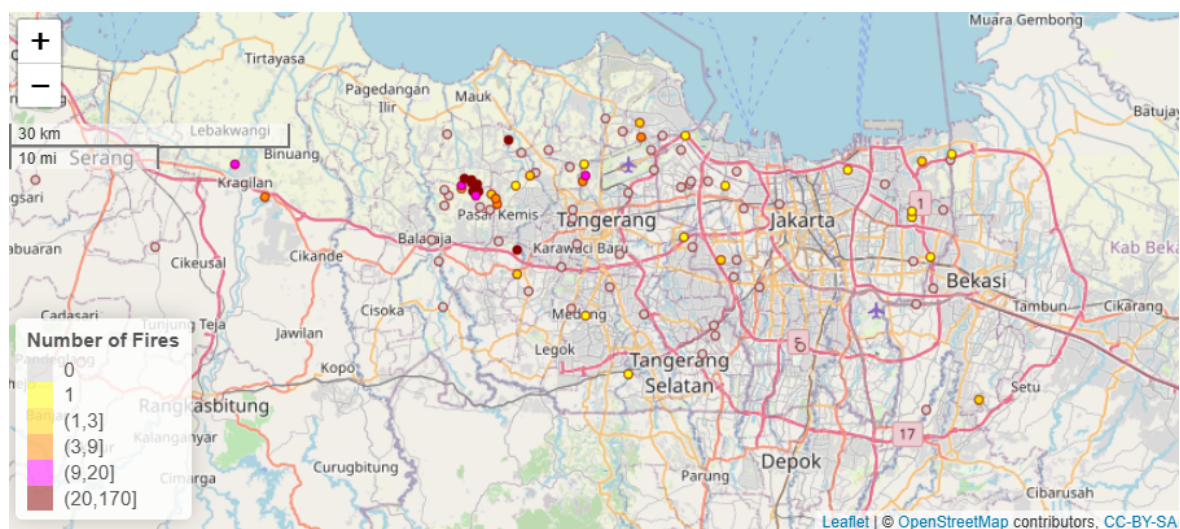


Figure S4: Zoomed-in map of Jakarta showing the number of fires detected by VIIRS overlapping with each GPW site in 2012-2019.

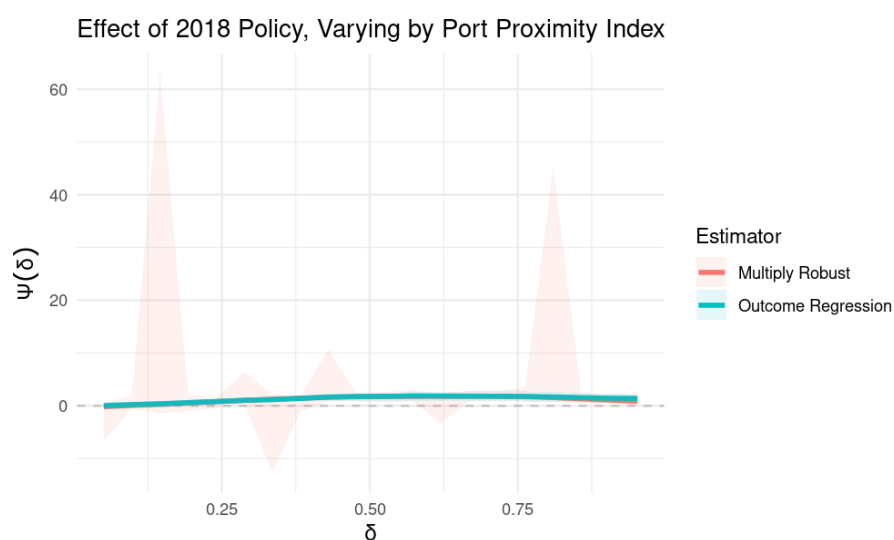


Figure S5: Main analysis run with LLKR bandwidth selected on all data (with repeated observations at each dump site).

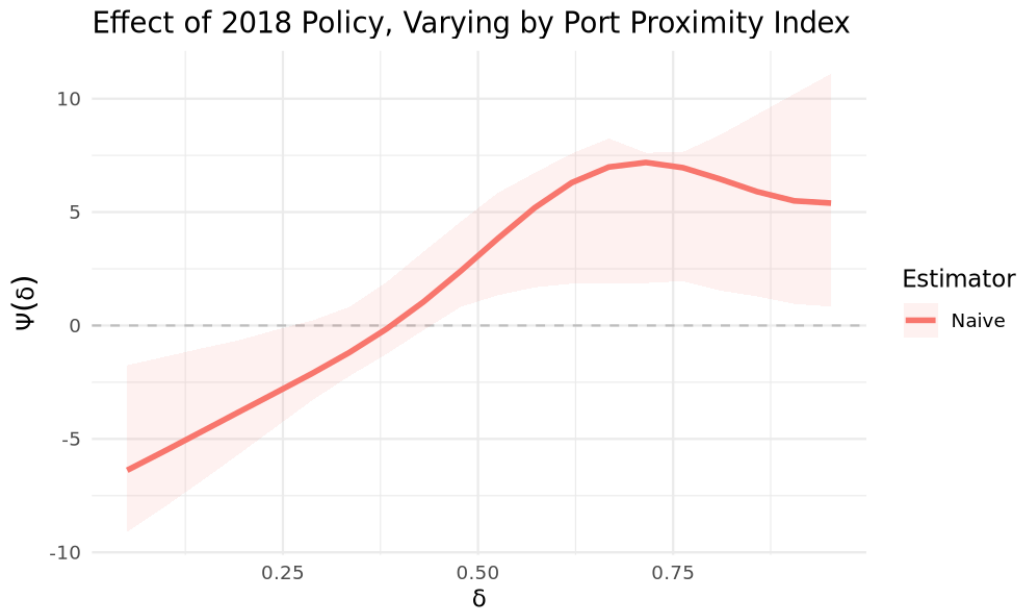


Figure S6: The confounder-naive results. Sampling bootstrap weights with spatial correlation (range=26.8km).

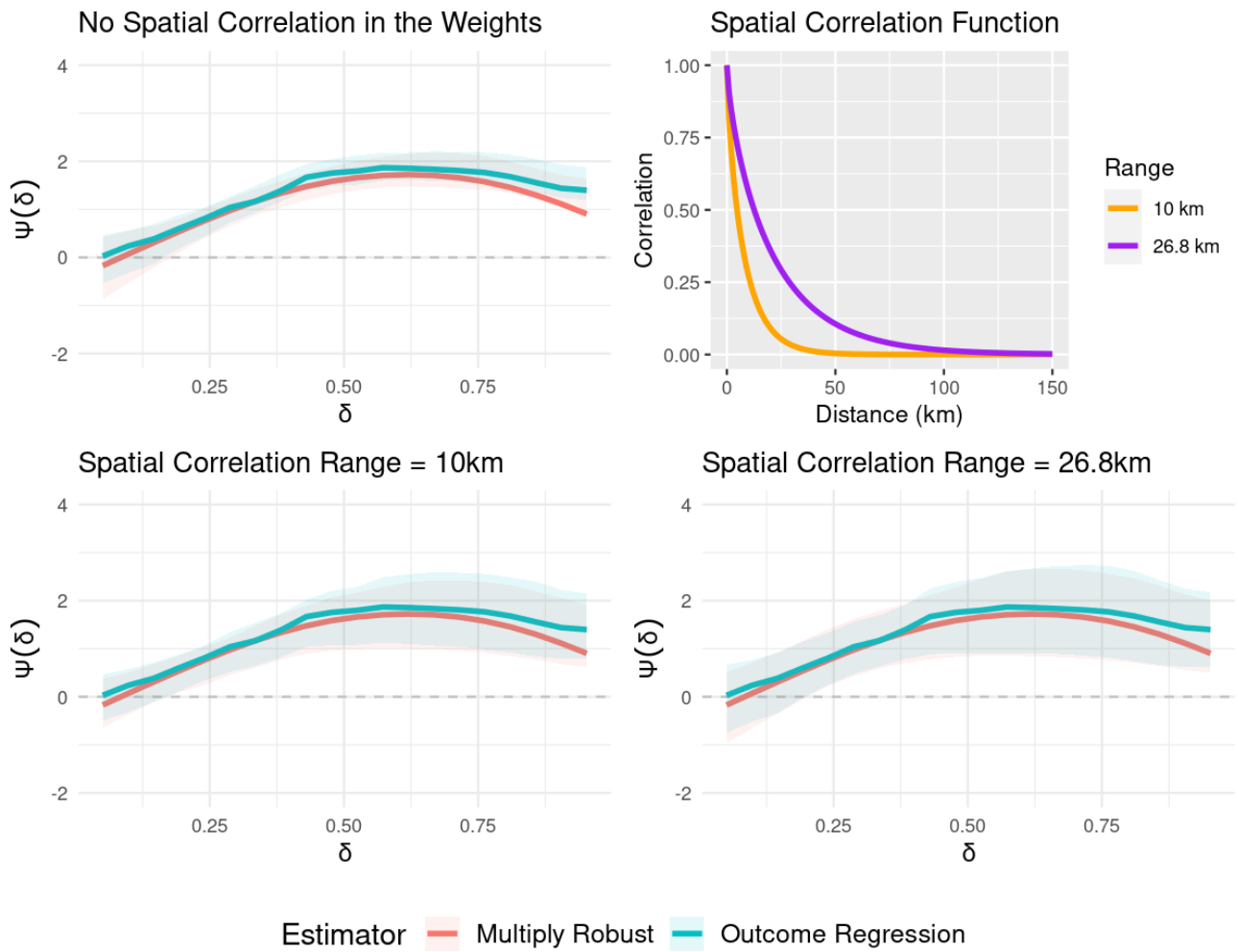


Figure S7: Comparing the results when the bootstrap weights have spatial autocorrelation range 0, 20, and 26.8 km respectively. The top righthand plot shows the Matérn correlation decay versus distance, using these different values for the range parameter.

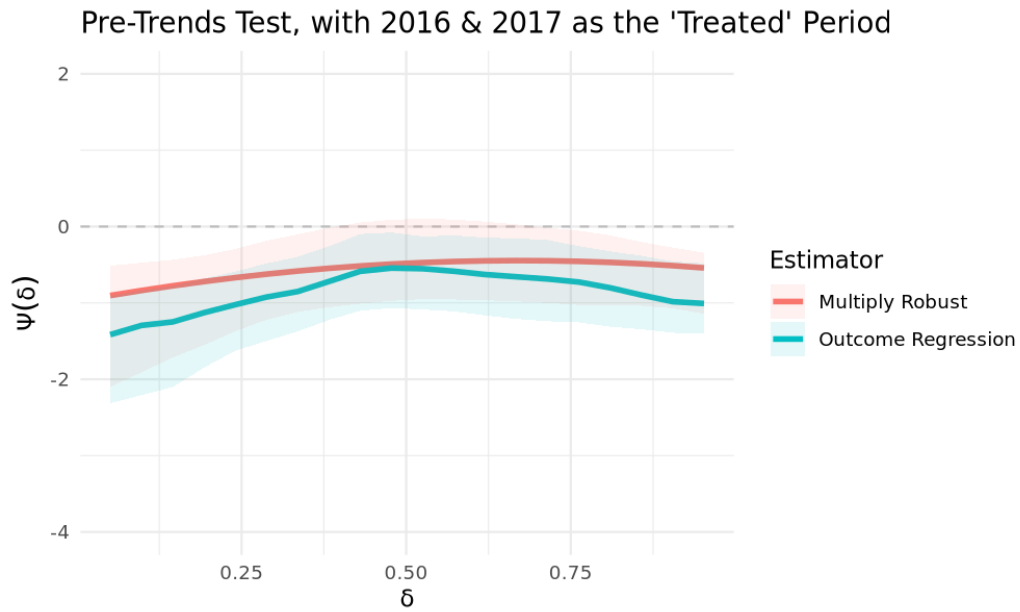


Figure S8: Pre-trends test for 2016-2017. Sampling bootstrap weights with spatial correlation (range=26.8km).

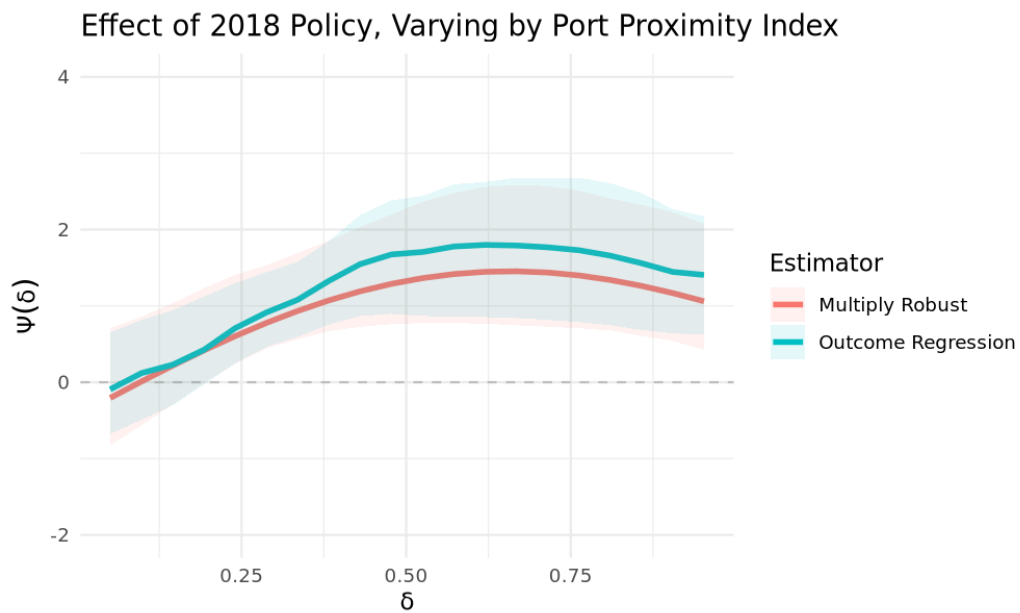


Figure S9: Sensitivity analysis including GPW site area as a covariate. Sampling bootstrap weights with spatial correlation (range=26.8km).

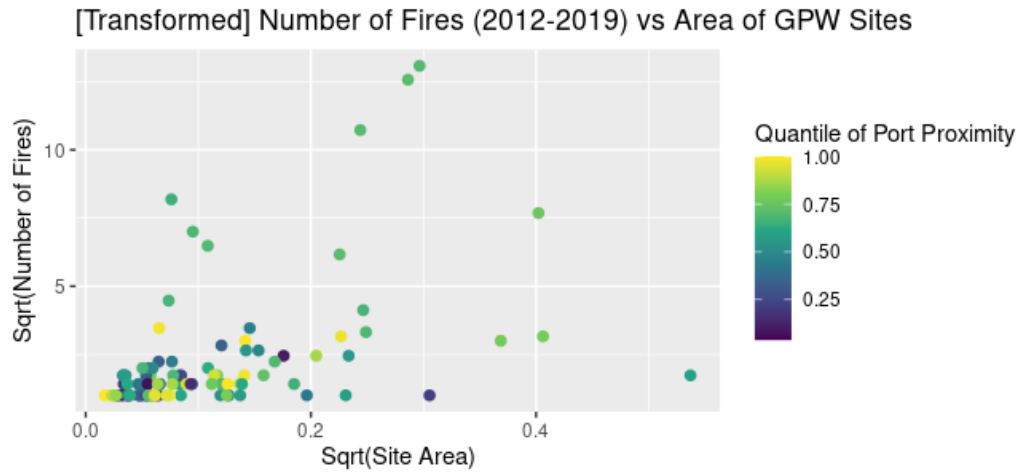


Figure S10: Square root of number of fires detected by VIIRS vs square root of GPW site area, colored by the quantile of port proximity.

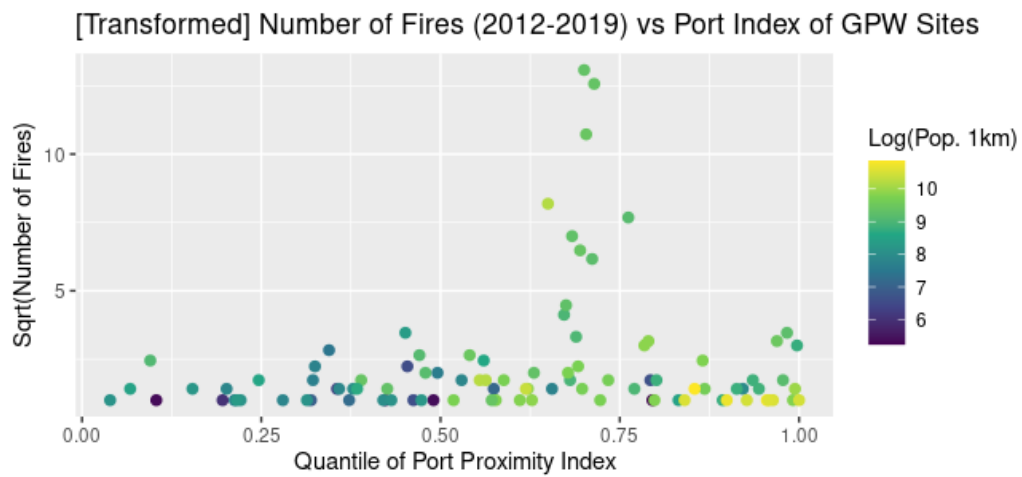


Figure S11: Square root of number of fires detected by VIIRS vs quantile of port proximity, colored by the log of population living within 1km of each GPW site.

C Simulations Exploring the Spatial Weighted Bootstrap

In this appendix, our primary aim is to evaluate the characteristics of the confidence intervals generated by our Spatial Weighted Bootstrap procedure, relative to those generated by a Non-spatial Weighted Bootstrap. Here, calculation of the ADT curve’s bias and Mean Absolute Error (MAE) is an intermediate step to better understand the confidence intervals, as Hettinger et al. (2025) present extensive investigation of a very similar ADT estimator.

To do this evaluation, we develop simulations which utilize the real (observed) exposure D and covariates \mathbf{X} to simulate the outcome Y .

C.1 Simulating the Outcome

First, we compute the mean function for the outcome data generating process using the real exposure and covariate data and setting “true” parameter values governing the relationship between these variables and the outcome in our simulated data. Our choice of these parameter values was guided by (a) using domain knowledge to select the sign of each coefficient, (b) producing an outcome distribution similar to that in the real data, and (c) producing a plausible ADT curve, similar to that observed in our main analysis.

The mean function for each location i and time t is given by:

$$\mu_{it} = B_t L_1(\mathbf{X}_{it}, D_{it}) + (1 - B_t) L_0(\mathbf{X}_{it})$$

where

$$L_0(\mathbf{X}_{it}) = -9.5 + 0.075(\text{Temp}_{it}) + 0.075(\text{Pop}_i) + 0.0001(\text{Temp}_{it})(\text{Pop}_i) + 0.15(\text{Time}_t) + 0.001(\text{Time}_t)(\text{Pop}_i) + 1(\text{Other_fires_province}_{it}) - 18(\text{Precip}_{it})$$

and

$$L_1(\mathbf{X}_{it}, D_{it}) = -12.5 + 0.075(\text{Temp}_{it}) + 0.075(\text{Pop}_i) + 0.0007(\text{Temp}_{it})(\text{Pop}_i) + 0.15(\text{Time}_t) + 0.001(\text{Time}_t)(\text{Pop}_i) + 1.5(\text{Other_fires_province}_{it}) - 20(\text{Precip}_{it}) + 2(D_{it}) \left[-3(D_{it}) + 0.4(\text{Pop}_i) + 0.2(\text{Time}_t) \right]$$

where “Temp” is temperature, “Pop” is population [density], “Time” is the fifth-root of the count of days since 01/01/2012, “Other_fires_province” is the fourth-root of the number of fires in the province not overlapping with any GPW site, and “Precip” is precipitation. For both L_0 and L_1 , we truncated any negative values ($\sim 0.06\%$) to zero post hoc.

We calculate the “true” ADT for each exposure value δ as

$$\Psi(\delta) = \frac{1}{96N} \sum_{i=1}^N \sum_{t=1}^{96} \left[L_1(\mathbf{X}_{it}, \delta) - L_0(\mathbf{X}_{it}) \right]$$

This true ADT curve is shown in Figure S12.

We simulate both spatially-structured and independent error in the outcome, as follows:

$$\tilde{Y}_{it} = \mu_{it} + \sigma_{\text{sp}} \epsilon_{\text{sp}} + \sigma_{\text{ind}} \epsilon_{\text{ind}}$$

where $\epsilon_{\text{sp}} \sim MVN(0, \Sigma)$, where the correlation function to generate the entries of Σ is $\text{Corr}(m; L) = \exp(-m/L)$ [Exponential form] and $\epsilon_{\text{ind}} \sim N(0, 1)$. The parameters L (the true spatial range), σ_{sp} , and σ_{ind} are constants, which we specify to obtain four distinct simulation scenarios:

1. Scenario 1: $L = 100$ km, $\sigma_{\text{sp}} = 2$, $\sigma_{\text{ind}} = 0.5$ (the “base case”)
2. Scenario 2: $L = 500$ km, $\sigma_{\text{sp}} = 2$, $\sigma_{\text{ind}} = 0.5$ (increased spatial range)
3. Scenario 3: $L = 100$ km, $\sigma_{\text{sp}} = 3$, $\sigma_{\text{ind}} = 0.5$ (increased spatial sigma)
4. Scenario 4: $L = 100$ km, $\sigma_{\text{sp}} = 2$, $\sigma_{\text{ind}} = 1.5$ (increased noise)

These four scenarios allow us to investigate the influence of different spatial error structures on the accuracy of our estimation and inference procedures. For each simulation scenario, we generate 100 simulated datasets (using 100 different seeds for random number generation), each having the same true parameter values and (real) exposure and covariates but different synthetic outcome variables.

C.2 Estimating the Effect Curve and Confidence Interval

When implementing our ADT estimation procedure on each simulated dataset, we correctly specify the outcome models' mean function but estimate the propensity score models π_B and π_D using Ranger (the same algorithm as in our main analysis).

When applying the Spatial Weighted Bootstrap, we fit both Exponential and Power covariance functions (the latter has correlation function $Corr(m; a, z) = 1 - zm^a$) to the empirical variogram of the residuals from the LLKR stage and use whichever model has the smaller RMSE to generate the spatial weights. As noted in Section 3.4.2, the spatial structure of the LLKR residuals is different than the spatial structure of the outcome (here, \tilde{Y}), so traditional notions of correctly vs incorrectly specifying the spatial correlation model do not directly apply here.

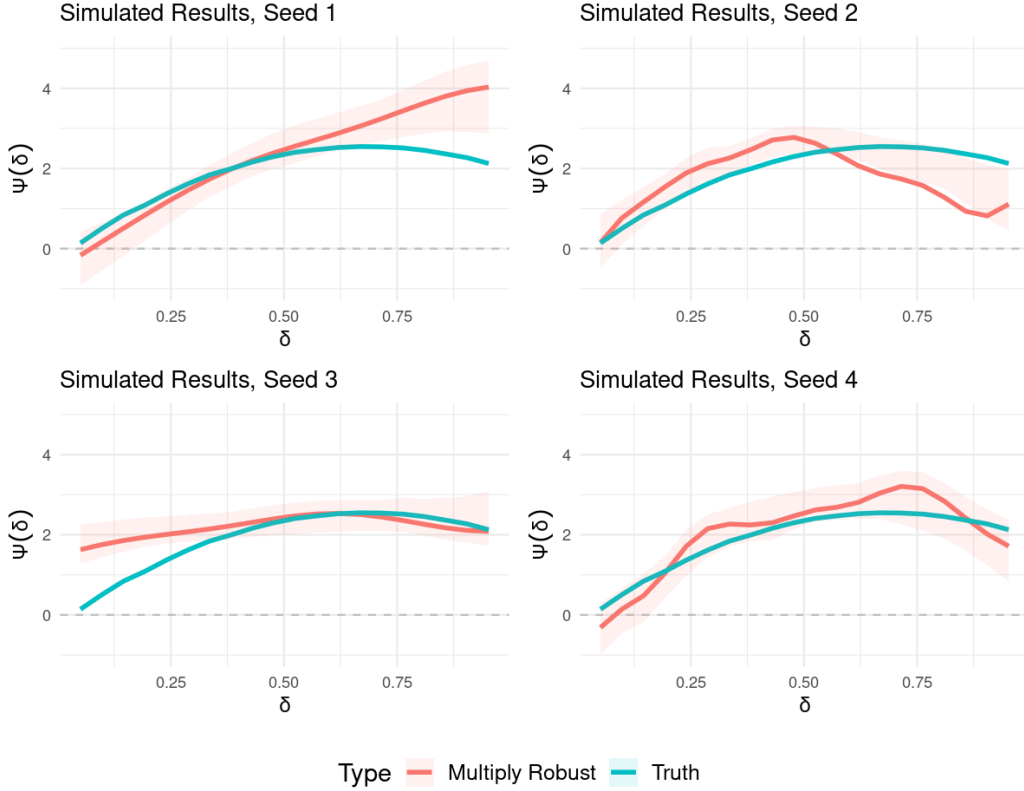


Figure S12: Examples of the ADT estimate from our multiply robust estimation procedure applied to (four instances of) simulated data from our base case scenario, compared to the true ADT curve.

C.3 Evaluating the Performance of the Spatial and Non-spatial Weighted Bootstraps

We compare our ADT curve estimates from each simulated dataset to the true ADT curve by computing the pointwise bias and MAE, which are then summarized by averaging across all 100 simulation replicates within each scenario. We then calculate the pointwise coverage and width of the 95% confidence intervals computed using the Spatial Weighted Bootstrap, and compare the results with those from a Non-spatial Weighted Bootstrap.

C.4 Simulation Results and Discussion

The bias and MAE results are shown in Figures S13 and S14, respectively. The confidence interval coverage and width results are shown in Figures S15 and S16, respectively.

First, we observe that the magnitude of the bias ranges between 0.1 and 0.5, while the true ADT ranges between 0.1 and 2.6, with an average value of 1.9. From the MAE plot, we see that the estimator is less stable on the tails (resulting in larger errors), which is to be expected for methods like LLKR. Our intuition is that the asymmetry of the true ADT curve contributes to the bias being higher at higher values of port proximity.

Note that in addition to the finite sample bias of LLKR, which results in imprecise centering of the ADT's confidence intervals (Hettinger et al., 2025), here we also do not know the correct specification of the

propensity score models π_B and π_D , instead estimating them from the data. Foreshadowing our coverage results, the simulations in Hettinger et al. (2025) indicate that misspecification of the propensity score models has a greater impact on coverage than misspecification of the outcome models.

In Figure S15, we see that neither the Spatial nor Non-spatial Weighted Bootstrap achieves 95% coverage at any value of δ (port proximity). However, the Spatial Weighted Bootstrap has consistently higher coverage than the Non-spatial method. This makes sense, as the Spatial method generates wider confidence intervals (as shown in Figure S16). Mirroring the results of the MAE plot, we see that the confidence interval coverage tends to be highest in the lower-middle range of δ (0.25-0.5) for both the Spatial and Non-spatial Weighted Bootstrap.

Now, we compare the differences in results across our four simulation scenarios. Note that both Scenario 2 (increasing L) and Scenario 3 (increasing σ_{sp}) generate greater similarity in the value of outcomes that are spatially proximate, through different mechanisms, relative to Scenario 1. Whereas, Scenario 4 simply increases the random noise in the outcomes.

In Figures S15 and S16, we see that inducing greater spatial signal (Scenarios 2 and 3) increases the width of the Spatial Weighted Bootstrap's confidence intervals, resulting in higher coverage. By contrast, the Non-spatial approach responds to increasing L by narrowing its confidence intervals (resulting in lower coverage) and responds to increasing σ_{sp} by widening its confidence intervals (resulting in higher coverage). In Scenario 4, the Spatial approach actually narrows its confidence intervals, likely because increasing σ_{ind} makes it harder to detect the spatially structured error, resulting in under-estimation of the spatial correlation.

In Figure S14, the only parameter configuration that stands out is Scenario 3 (increased σ_{sp}), which results in higher MAE (lower precision in the point estimate) across values of δ . In Figure S13, none of the configurations have consistently different bias.

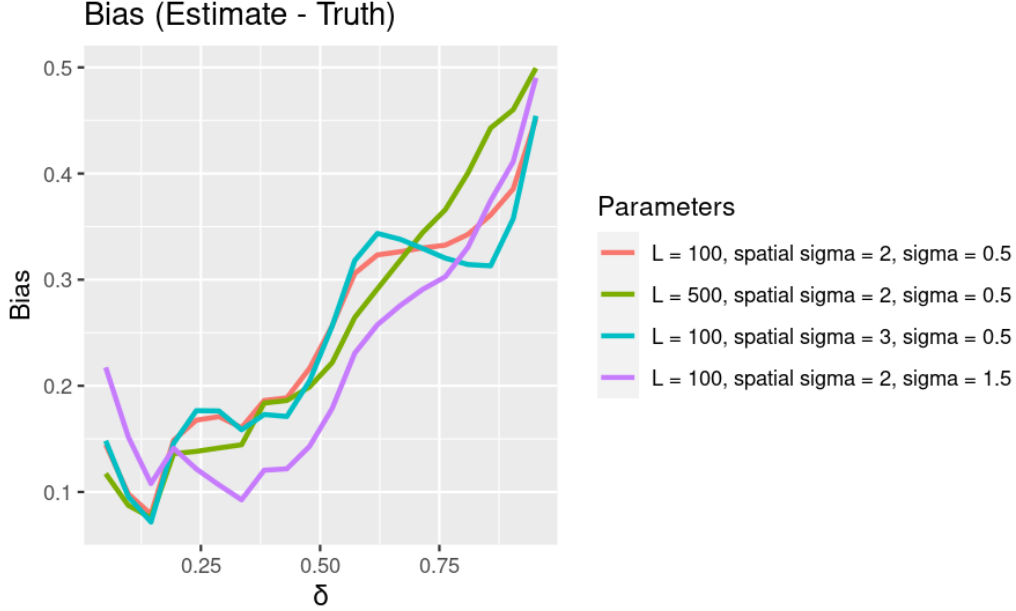


Figure S13: Bias of the estimated ADT compared to the true ADT in our simulations.

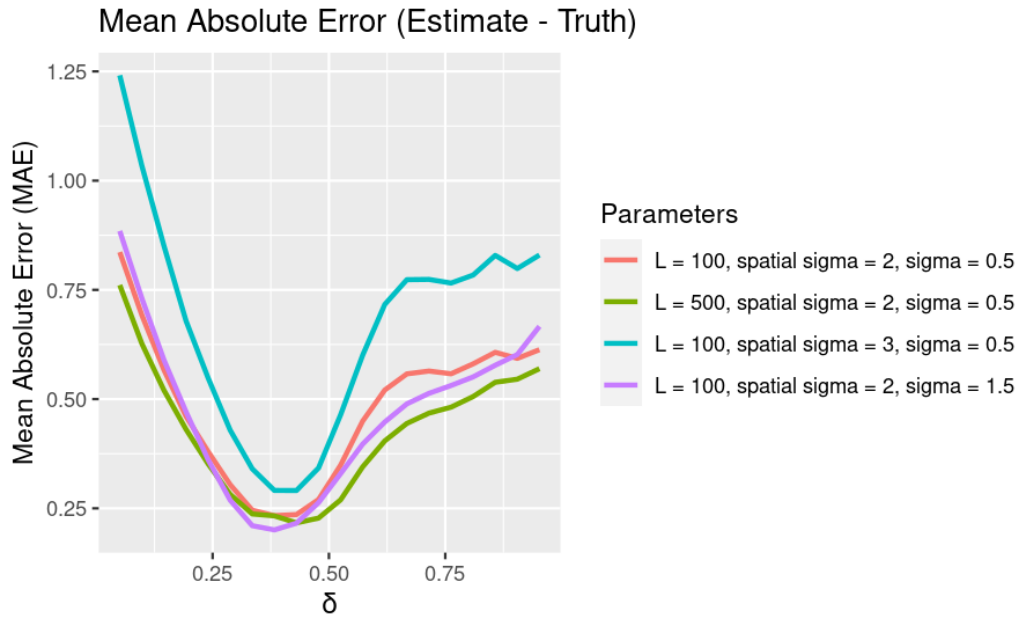


Figure S14: Mean Absolute Error (MAE) of the estimated ADT compared to the true ADT in our simulations.

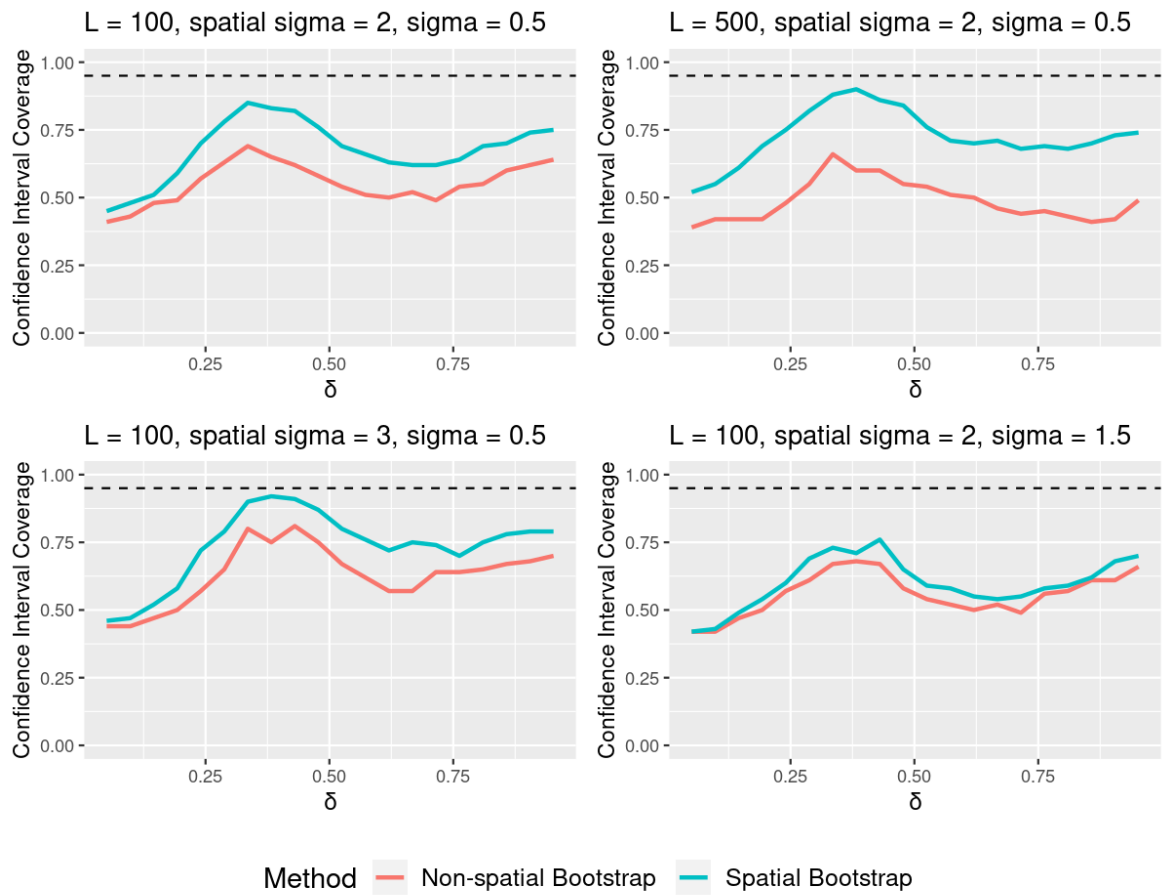


Figure S15: Coverage of the 95% confidence intervals in our simulations. The dashed line indicates the desired 95% coverage.

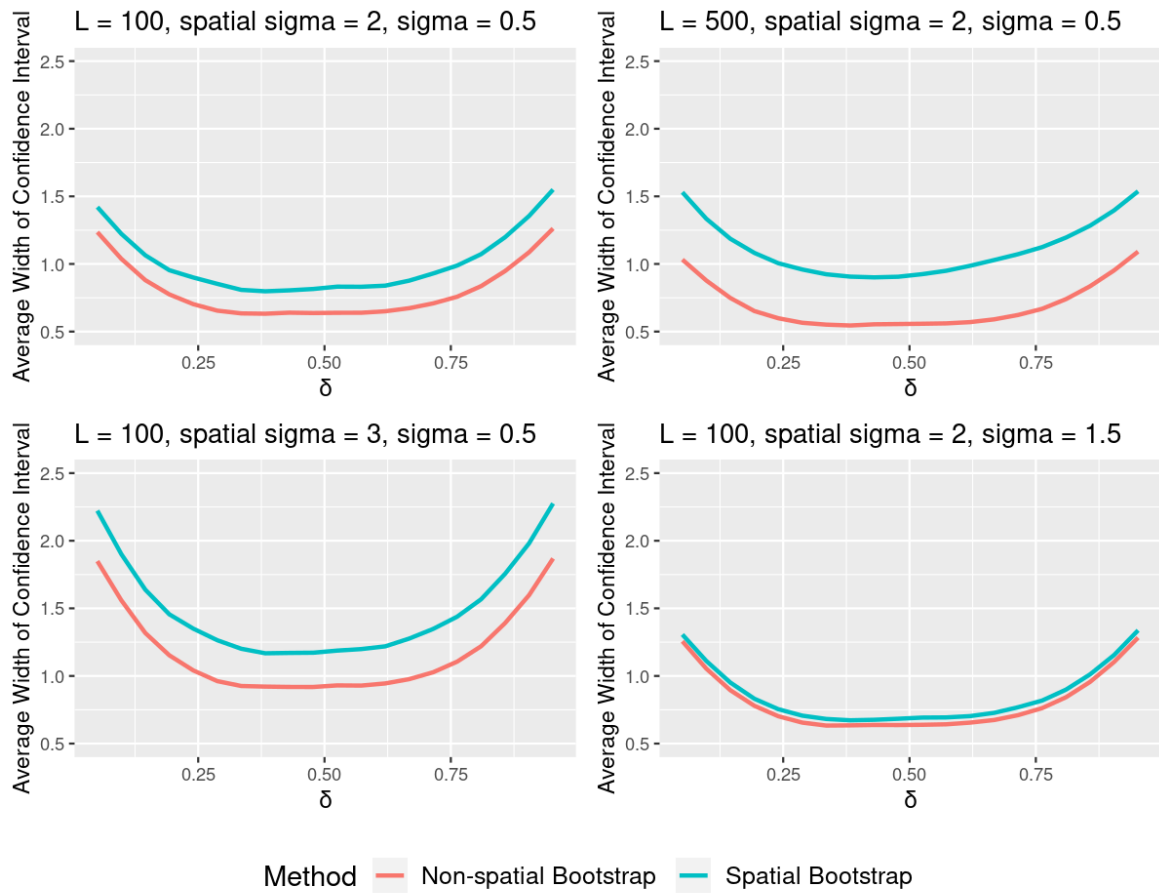


Figure S16: Width of the confidence intervals in our simulations.